공학박사 학위논문

Tearing Modes during Tokamak Plasma Current Ramp Up

토카막 플라즈마 전류 상승기의 찢어짐 모드

2019 년 2 월

서울대학교 대학원

에너지시스템공학부

양 정 훈

Tearing Modes during Tokamak Plasma Current Ramp Up

지도 교수 황 용 석

이 논문을 공학박사 학위논문으로 제출함

2018 년 10 월

서울대학교 대학원

에너지시스템공학부

양 정 훈

양정훈의 공학박사 학위논문을 인준함

2018 년 12 월

위 원 장	함 택 수	(인)
부위원장	황 용 석	(인)
위 원	김 재 현	(인)
위 원	나 용 수	(인)
위 원	윤 건 수	(인)

Abstract

Tearing Modes during Tokamak Plasma Current Ramp Up

Jeong-hun Yang
Department of Energy System Engineering
The Graduate School
Seoul National University

Tokamak is a concept to confine a plasma using the magnetic field and plasma current to extract the nuclear fusion energy. A fast plasma current ramp up is reportedly obstructed by a magneto-hydrodynamic plasma instability assumed to be a tearing mode excited by the hollow current density profile produced by the skin effect from the fast time-varying driving loop voltage. To test the assumption, a comprehensive diagnostics of the instability at the low temperature, transient phase of the plasma current ramp up is needed. An internal magnetic probe is used for the direct measurement of the magnetic islands in the low temperature plasmas where the perturbation is small. Previously, the interpretation of the measurements was difficult since a reliable equilibrium flux surface information was not available at small devices compatible with the internal magnetic probes. During the plasma current ramp up in a VEST (Versatile Experiment Spherical Torus) discharge, a distinctive instability pattern arises in the spectrogram of the Mirnov coils. In this dissertation, the instability during a tokamak plasma current ramp up is studied.

VEST (Versatile Experiment Spherical Torus) is a spherical torus with the major radius of 0.4 m, the minor radius of 0.3 m, the on-axis toroidal field of 0.1 T and the

plasma current of 0.1 MA. The TF coil is powered by an ultracapacitor bank and the PF coils are powered by the capacitor banks switched at the pre-programmed times. The PEV injects a prefill gas prior to the loop voltage application. Magnetic diagnostics in VEST are placed inside and outside the plasma. Total 11 flux loops and 49 magnetic probes are distributed along the poloidal plane. Flux loops are sampled at 25 kS/s, while magnetic probes are sampled at 250 kS/s. Equilibrium flux surfaces link various diagnostics into a single frame. The equilibrium reconstruction code VFIT is developed to implement the algorithm of the free boundary solution of the Grad Shafranov equation. Real data includes noise and signal that need to be separated carefully. A set of 12 squared elements are used to model the plasma current distribution, and the currents of each elements are used as a coil current equivalent for the computation of the wall current by the plasma current. In the VFIT run, the sensor signals are fit to 10% on average and the convergence criteria is set to 10^{-3}. Useful equilibrium parameters can be post-processed from the reconstructed equilibrium flux surfaces. Mode information of a magnetic fluctuation bears the characteristics of the instability. Toroidal array of 2 Mirnov coils are Fourier analyzed to determine the toroidal mode number and the frequency. Poloidal array of 25 Mirnov coils are singular value decomposed to determine the poloidal mode number. The mode identification is performed every 0.2 ms, within 1 ms time window. In VEST, the plasma current decrease with the internal magnetic probes is no more than 10%, presumably because of the small plasma size and energy. A sensor group is composed of a Hall sensor and two chip inductors, and total 8 sensor groups cover $R > 0.30$ m with the spatial resolution $\Delta R = 0.05$ m on midplane. Mount of the internal magnetic probes is provided by a printed circuit board. Enclosure for the internal magnetic probes includes the stainless steel pipes and alumina tube to provide the electrostatic and thermal insulation respectively. Calibration of the

internal magnetic probes includes three steps: Helmholtz coil, misalignment angle, and radial position.

A magnetic island in a tokamak can produce a characteristic dB_Z/dt structure. Internal magnetic probe measurements shows the phase reversal structure, supporting the magnetic island existence. Phase reversal and island chain location measured using the internal and external magnetic diagnostics are in good agreement. Then, the dynamics of the magnetic islands can be studied using the internal magnetic probes. Two magnetic islands are onset simultaneously, are phase locked to each other, and move to the inboard with the bulk plasma. The magnetic islands moving together as they are phase locked is intriguing since the previous understandings were that the adjacent island would merge. The magnetic island width is generally related to the external Mirnov coil signals with the calibration factor determined from a direct measurement of the island. Then, the island width can be estimated from the external Mirnov coil signal when the internal magnetic probes are removed.

The classical tearing mode theory explains the response of the tearing mode to the current ramp rate control. Control of the variables prefill gas pressure and wall condition is acceptable. To further clarify the interpretation based on the classical tearing mode theory, an experiment is designed to control the local magnetic shear itself. The onset and suppression of a (m,n) mode coincides with the change in the magnetic shear dq/dr at the $q = m/n$ surface, as predicted by the classical tearing mode theory. Although the classical tearing mode theory explained the tearing mode response to the current ramp rate control, the theory fails to explain the tearing mode response to the prefill gas pressure control. Control of the variables plasma current ramp rate and plasma shaping factor is acceptable. Comparing the Pearson correlation coefficients, the prefill gas pressure is a control knob as effective as the current ramp rate for the tearing mode control. It is presumed that in VEST, the

neoclassical tearing mode theory may explain the response of the tearing mode during a plasma current ramp up to the control knobs of current ramp rate and prefill gas pressure.

Island width evolution is in general modelled by the modified Rutherford equation. VFIT and PEST-3 are used to compute the variables in the modified Rutherford equation. The 2/1 mode island width evolution is followed, assuming a constant small island effect factor $w_{small} = 6\,\mathrm{cm}$. Modelled and measured 2/1 mode island width evolution are in good agreement, supporting the neoclassical tearing mode existence. The specific mode number combination of the coexisting magnetic islands in VEST, at first the 2/1 + 3/2 and then the 3/1 + 4/2 modes, supports the neoclassical tearing mode existence. The observation of the fluctuation asymmetry would support the existence of two magnetic islands by the neoclassical tearing mode excitation. The fluctuation asymmetry is observed in the internal magnetic probe and external Mirnov coil measurements. Previously, the validity of the observations was unclear however since there were no internal measurements to confirm. Filament model of a magnetic island is used for the modelling of the fluctuation asymmetry. The combination of 4/2 + 3/1 instead of 2/1 + 3/2 magnetic islands is modelled with reasonable accuracy. The poloidal distribution of Mirnov coil signals from the measurements and the reconstruction using the filament modelling are in good agreement, supporting the existence of two magnetic islands by the neoclassical tearing mode excitation. The $l_i - q_a$ empirical stability diagram assumes that the instability during a tokamak plasma current ramp up is the classical tearing mode, and apparently fails to explain some stable shots located outside the stable region. Based on the experimental results, the stable region becomes wider at lower β_N and narrower at higher β_N. Then, the lower internal inductance startup is available if the normalized beta is kept low enough to avoid the neoclassical tearing mode excitation.

Keywords: Tokamak startup.
VEST.
Internal magnetic probes.
Equilibrium reconstruction.
Magnetic islands.
Tearing modes.
Modified Rutherford equation.
Fluctuation asymmetry.
Neoclassical tearing modes.
$l_i - q_a$ stability diagram.

Student Number: 2013-30996

Contents

List of Figures

List of Tables

Chapter 1. Introduction

1.1. Motivation

Nuclear fusion [1] is one of the highly sought after future energy sources. Tokamak [2] is a concept to magnetically confine and heat a plasma to a temperature sufficiently high for a significant nuclear fusion reaction, which have been leading the nuclear fusion research since the demonstration of a high temperature plasma [3].

Plasma current is essential in confinement and heating of a tokamak plasma. Since a transformer action induces the plasma current in most tokamaks, an efficient plasma current ramp up is linked directly to the extended pulse length of a tokamak through the spendable volt-seconds of the transformer. A fast plasma current ramp up, however, is reportedly obstructed by a magneto-hydrodynamic plasma instability [4]. This instability is assumed to be a tearing mode [5] excited by the hollow current density profile produced by the skin effect from the fast time-varying driving loop voltage. At the plasma current ramp up the plasma stored energy and hence the bootstrap current fraction [6] is assumed to be low, excluding the excitation of the neoclassical tearing modes [7]. Therefore, the empirical stability diagram as shown in Figure 1.1 is generally used to analyze the instability during a tokamak plasma current ramp up with only the current density profile parameters: internal inductance (l_i, related to peakedness) and edge safety factor (q_a, related to scale) [8]. However, experiments show that there are at least three other parameters which also affect the stability during tokamak plasma current ramp up: prefill gas pressure [9], plasma shape [10], and wall condition [4], in which these “other” control knobs are assumed to work indirectly by affecting the current density profile.

The assumptions on the instability during a tokamak plasma current ramp up were not tested before due to the difficulty of the diagnostics. These assumptions include the existence of magnetic islands which proves that the instability is a tearing mode, the classical nature of the tearing modes and the mechanism of the control knobs on the instability. To test these assumptions, a comprehensive diagnostics of the instability at the low temperature, transient phase of the plasma current ramp up is needed.

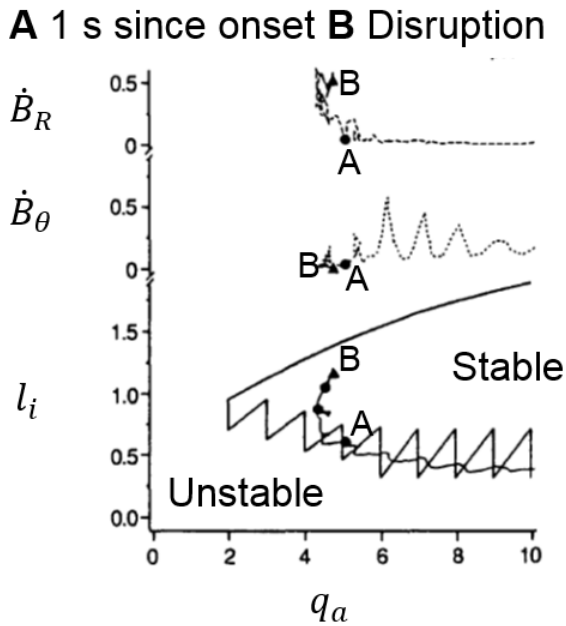

Figure 1.1 Stability analysis of a JET discharge in the internal inductance (l_i) – edge safety factor (q_a) operating space, compared with the poloidal ($\dot{B}_\theta$) and radial ($\dot{B}_R$) magnetic fluctuations. As plasma current is ramped up (q_a decreased), this discharge goes through the region labeled "unstable" in the $l_i - q_a$ space, which may have caused the peaking of $\dot{B}_\theta$, eventually leading to a disruption between time A and B (characterized by the sudden increase in $\dot{B}_R$) [8].

Magnetic islands naturally emerge from a tearing mode excitation [5]. The width of a magnetic island is generally related to the external Mirnov coil signals with the calibration factor determined from a direct measurement of the island [11], most commonly by the electron cyclotron emission (ECE) radiometry. However, the ECE radiometry requires a high plasma temperature [12] for a high signal to noise ratio, while the plasma temperature is low during the tokamak plasma current ramp up. On the other hand, an internal magnetic probe is generally avoided in high temperature plasmas since the inserted insulator reportedly absorbs the plasma energy [13] and perturbs the plasma, while in low temperature plasmas the perturbation is small [14] and may provide the direct measurement of the magnetic islands.

Internal magnetic probes have been used for the diagnostics of the instability during a plasma disruption in LT-3 [15] and TORTUS [16] and during a plasma current ramp up in TOSCA [17] and SUNIST [18]. In addition to the current density profiles shown in Figure 1.2, the fluctuation of the poloidal and radial magnetic fields have been measured to reveal a good direct picture of the plasma during a tearing mode instability. However, the interpretation of the measurements was difficult without a reliable equilibrium flux surface information, which was not available at small devices compatible with the internal magnetic probes where the plasma current is small and the currents flowing in the vacuum vessel walls or outside the last closed flux surface significantly limit the signal to noise ratio of the magnetic diagnostics, especially at the transient phase during plasma current ramp up.

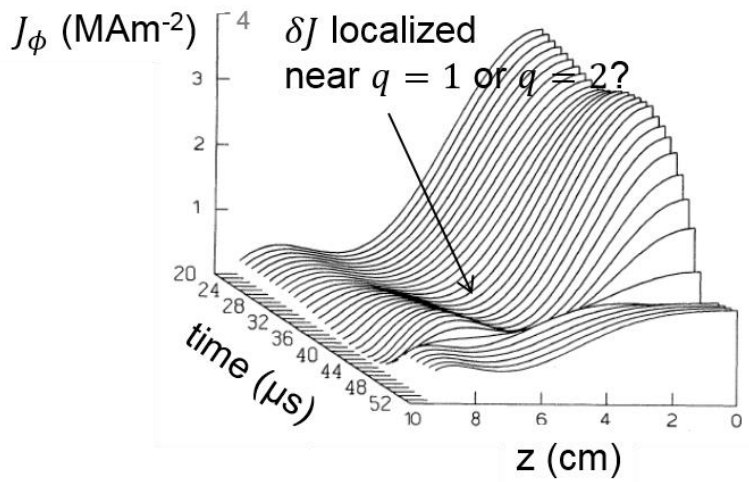

Figure 1.2 Current density profile of a LT-3 discharge during a plasma disruption. The current density profile is strongly peaked on axis at 24 μs, falls slightly then recovers at 32-40 μs, and disrupts to a flatter distribution at 48 μs. The perturbation in the current density profile is related to the locations of the $q=1$ or $q=2$ surfaces. The current density and the safety factor profiles are deduced from the internal magnetic probe measurements [15].

1.2. Objectives

During the plasma current ramp up in a VEST (Versatile Experiment Spherical Torus) [19] discharge, a distinctive pattern arises in the spectrogram of the Mirnov coils as shown in Figure 1.3. At least two modes are onset at approximately 0.304 seconds, before the plasma current attains the maximum of this discharge at 0.306 seconds, and the frequencies drop together from 30/15 to 12/6 kHz afterwards.

In this dissertation, the instability during a tokamak plasma current ramp up is studied. The internal magnetic probes are used along with the external magnetic diagnostics to provide the cross referenced and comprehensive picture of the instability. Then, the measurements are interpreted based on the modellings, with the primary goal to identify the mode characteristics and to determine if the mode is the classical tearing mode as assumed. From the study, the means to avoid or even suppress the instability may be explored, which will help the understanding of a tokamak operation, especially during the plasma current ramp up.

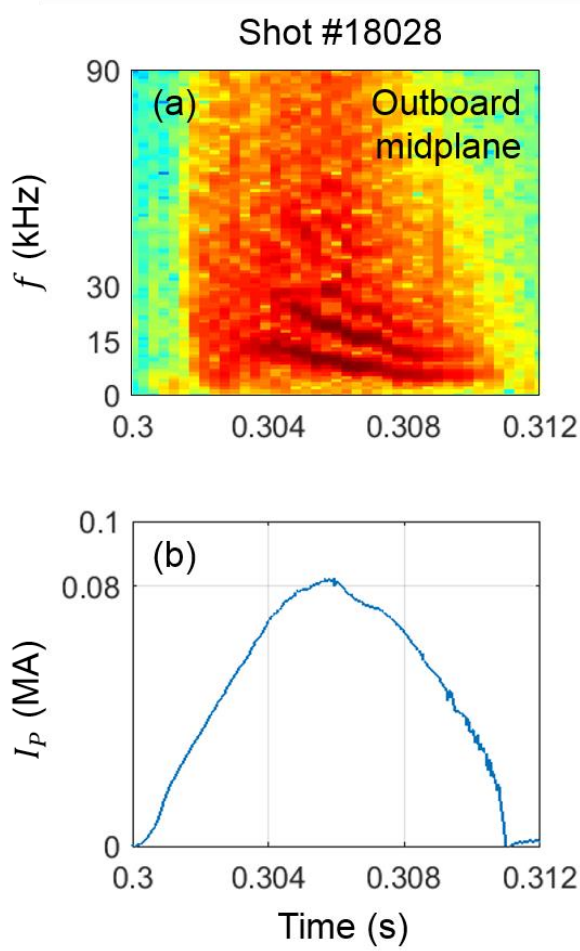

Figure 1.3 Instability of a VEST discharge during a plasma current ramp up. (a) Spectrogram of a Mirnov coil located at the outboard midplane showing a distinctive pattern. (b) Plasma current. At least two modes are onset at approximately 0.304 seconds, before the plasma current attains the maximum of this discharge at 0.306 seconds, and the frequencies drop together from 30/15 to 12/6 kHz afterwards.

Chapter 2. VEST Device

2.1. Ohmic discharge

VEST (Versatile Experiment Spherical Torus) [19] is a spherical torus with the major radius of 0.4 m, the minor radius of 0.3 m, the on-axis toroidal field of 0.1 T and the plasma current of 0.1 MA. The schematic of a poloidal plane in VEST is shown in Figure 2.1, where the poloidal field (PF) coils, the tungsten limiter, the stainless steel vacuum vessel, and the piezoelectric valve (PEV) for the prefill gas injection are labeled. The typical operation of VEST is shown in Figure 2.2, where the PF coil switching times, the TF coil switching times, the electron cyclotron heating (ECH) pre-ionization time, and the PEV operation time are labeled.

The TF coil is powered by an ultracapacitor bank and the PF coils are powered by the capacitor banks switched at the pre-programmed times. PF05 is used for the formation of the trapped particle configuration which enables a more efficient ECH assisted startup [20]. PF06 and PF10 are placed above and next to the main discharge chamber in order to provide a flexible equilibrium field to control the plasma shape and position. PF01 is switched three times: C1 charges up the coil with current, C2 swings down to provide a loop voltage for a tokamak plasma startup, and C3 provides extra volt-second to persist the driving loop voltage. It is noteworthy that the plasma current ramp rate can be controlled by changing the C2 capacitance. The specifications of the PF coil system are summarized in Table 2.1 and Table 2.2.

The PEV injects a prefill gas prior to the loop voltage application. The main gas used in VEST is hydrogen (H_2). It is noteworthy that the prefill gas pressure can be controlled by changing the PEV open time.

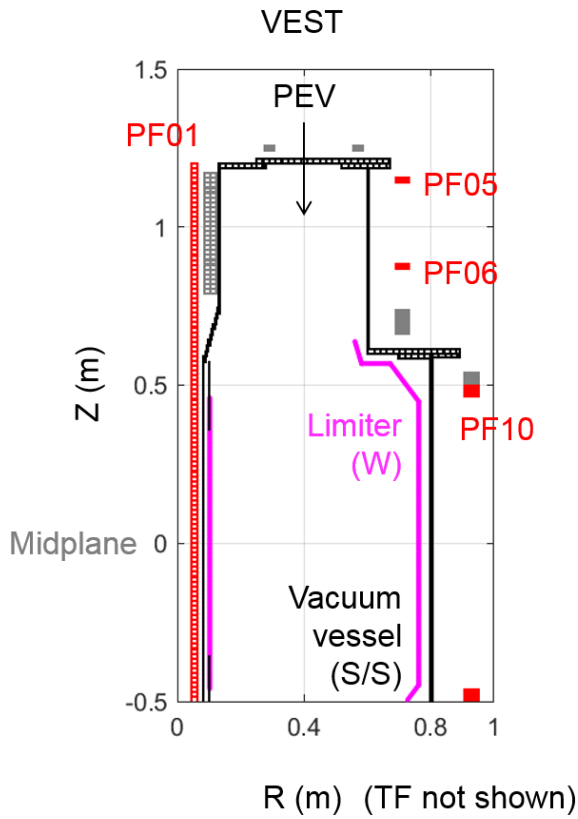

Figure 2.1 Schematic of a poloidal plane in VEST. Vacuum vessel are colored in black. Active PF coils are colored in red, whereas inactive PF coils are colored in grey. Limiters are colored in magenta.

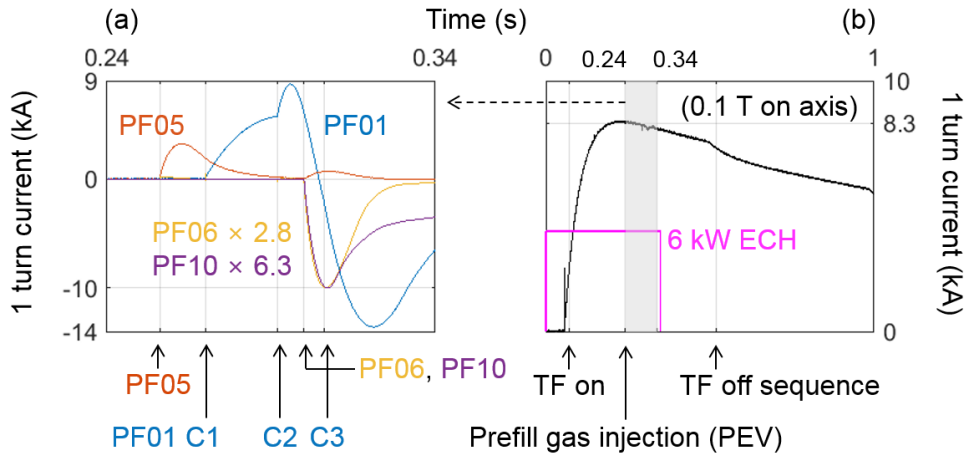

Figure 2.2 Typical operation of VEST. (a) PF coil current waveforms during the PF operation time. (b) TF coil current waveform with ECH power injection time (boxed) and PF operation time (shadowed) overlaid. Note that an entire shot sequence takes 1 s, within which the plasma current is expected at 0.3 s.

Table 2.1 Specifications of VEST PF coil system: Coil properties. The radial (r) and vertical (z) positions, the vertical coil width (w), the electric resistance (R) and inductance (L), and the number of turns (n) are summarized. The electrical properties are measured using Fluke PM6304 RLC meter at 100 Hz when the upper and lower coils are connected in series.

Coil	r (m)	z (m)	w (mm)	R (mΩ)	L (mH)	n
PF01	0.053	0.000	2385	210	1.51	632
PF05	0.710	1.150	8	175	0.75	24
PF06	0.710	0.875	8	160	0.83	24
PF10	0.930	0.475	24	644	3.85	48

Table 2.2 Specifications of VEST PF coil system: Power supply properties. The switching time (SW), the charging voltage (V) and the capacitance (C) are summarized. All switches except PF05 are silicon controlled rectifier (SCR) based, and PF05 switch is insulated-gate bipolar transistor (IGBT) based.

Coil	SW1	SW2 (ms)	SW3	V1	V2 (V)	V3	C1	C2 (mF)	C3
PF01	470	492	506	850	2800	2800	260	14	115
PF05		456 – 470			900			45	
PF06		500			1140			45	
PF10		500			1700			9	

2.2. External magnetic diagnostics

Magnetic diagnostics in VEST are placed inside and outside the plasma. The details of the internal magnetic diagnostics are presented in Section 2.3.

The location of the external magnetic diagnostics sensors are shown in Figure 2.3 and Figure 2.4. Total 11 flux loops are distributed along the poloidal plane and measures the loop voltage near the plasma surface. Total 49 magnetic probes are placed at section b (inboard) and J (outboard), with an additional 2 magnetic probes placed at section K (outboard). The cutoff of the magnetic probes is 94 kHz, determined by the 0.5 mm thick (d) stainless steel shield plate, with the effective radius (r) of 4 mm derived from the plate being located 8 mm clear from the vacuum vessel wall, and computed using the relation for a cylindrical conducting shield

$$f = \frac{1}{\pi r d \mu \sigma} \tag{2.1}$$

where μ is the magnetic permeability and σ is the electric conductivity. The double filtered Miller analog integrators are inserted in 25 magnetic probes, in evenly distributed groups throughout the poloidal plane. The grouping is for the redundancy. The remaining 24 magnetic probes and the 2 off-plane magnetic probes are in the Mirnov configuration (i.e. without integrator).

The digitization scheme of the external magnetic probes is shown in Figure 2.5. Flux loops are sampled at 25 kS/s, while magnetic probes are sampled at 250 kS/s. The signals from the integrated magnetic probes and the flux loops are used for the equilibrium reconstruction (Section 2.2.1), and the signals from the Mirnov coils are used for the fluctuation measurement (Section 2.2.2).

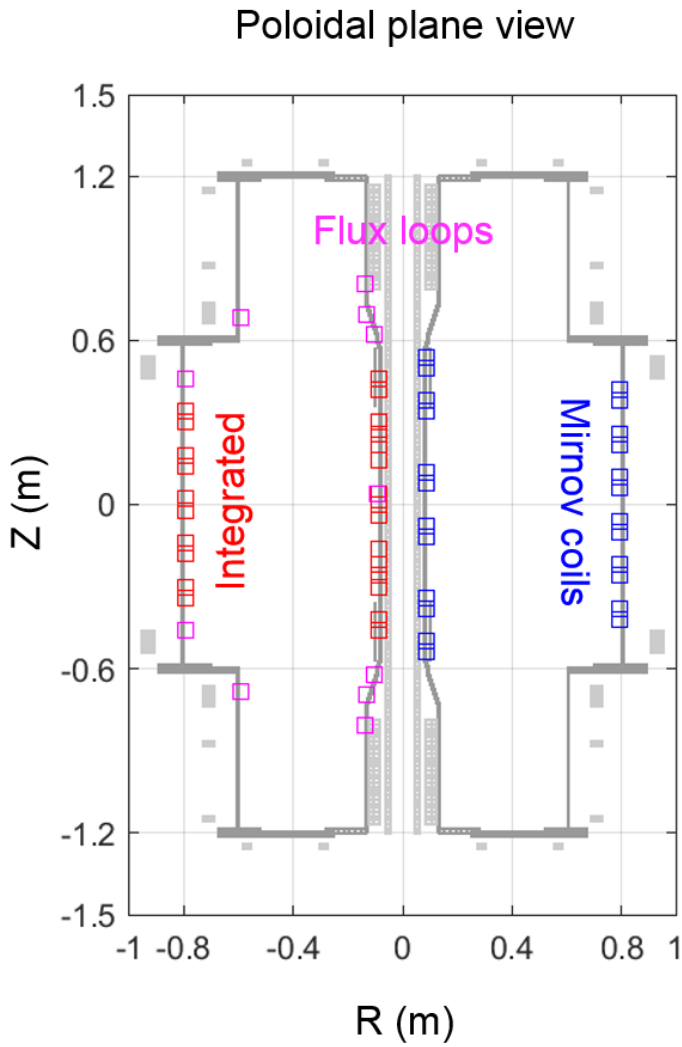

Figure 2.3 Location of the external magnetic diagnostics sensors: Poloidal plane view. Flux loop locations are colored in magenta. Locations of the magnetic probes with and without the analog integrator are colored in red and blue respectively.

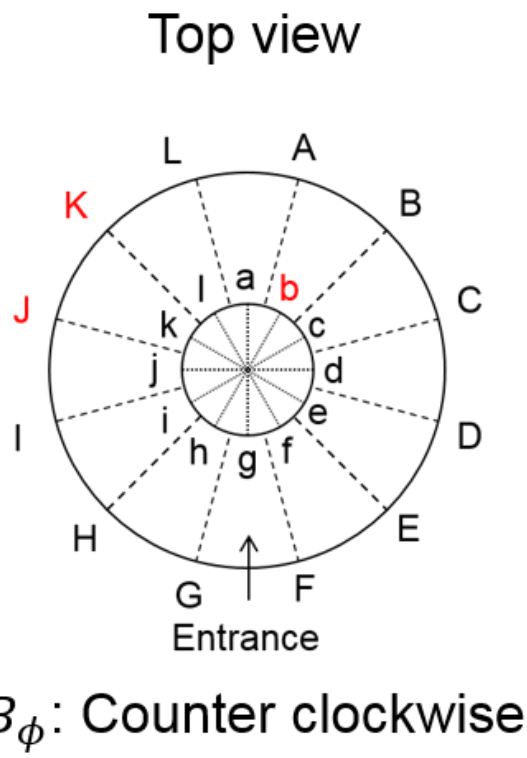

Figure 2.4 Location of the external magnetic diagnostics sensors: Top view. The highlighted sections K, J and b are where the external magnetic diagnostics sensors are located.

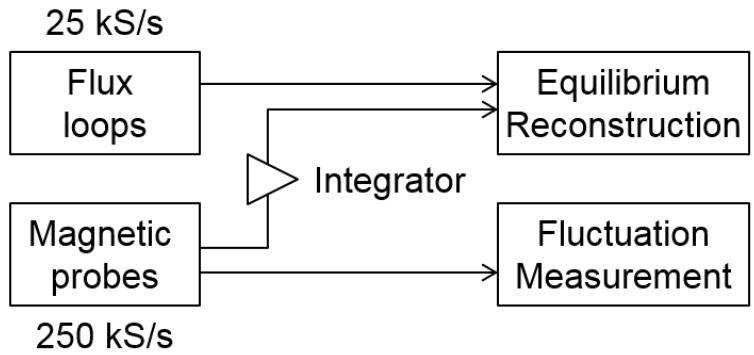

Figure 2.5 Digitization scheme of external magnetic probes. Left column lists the sensors, and right column lists the purpose. Flux loops are sampled at 25 kS/s, while magnetic probes are sampled at 250 kS/s.

2.2.1. Equilibrium reconstruction

Equilibrium flux surfaces link various diagnostics into a single frame. A general method to determine the equilibrium flux surfaces from a typical tokamak magnetic diagnostics involves a free boundary solution of the Grad Shafranov equation [21]. This method also provides the safety factor profile essential for the instability study, unlike the filament [22] or element [23] based fitting methods.

In an axisymmetric cylindrical coordinates (R,ϕ,Z),

$$\Delta^*\psi = -\mu_0 R J_\phi \tag{2.2}$$

where the operator $\Delta^* \equiv R^2\nabla\cdot\left(\nabla/R^2\right)$ relates the poloidal flux ψ which is used to label the equilibrium flux surfaces and the current density J. The polynomial representation of the toroidal current density is

$$J_\phi = Rp' + FF'/\mu_0 R = \sum \alpha_n R^\nu \psi_N^n \tag{2.3}$$

where p' and FF' are closely related to the pressure and toroidal flux and the arbitrary functions of the normalized poloidal flux $\psi_N \equiv (\psi-\psi_a)/(\psi_b-\psi_a)$ where ψ_a and ψ_b are the poloidal flux at magnetic axis and plasma boundary respectively, and α_n are the coefficients of n-th order polynomials. Note that $\nu=1$ for p' coefficients and $\nu=-1$ for FF' coefficients [24]. At each step of iterative solution of Equation (2.2), the coefficients α_n are updated to minimize

$$\chi^2 = \sum\left[(M_i - C_i)/\sigma_i\right]^2 \tag{2.4}$$

where M and C are measured and computed sensor signals respectively and σ is the measurement uncertainty.

The equilibrium reconstruction code VFIT is developed to implement the algorithm in the previous paragraph. To validate the implementation, first a set of

sensor signals is generated from an analytic equilibrium (exact solution) with the current density

$$J_\phi = \lambda\left(\beta\frac{R}{R_g} + (1-\beta)\frac{R_g}{R}\right)\left(1-x^2\right)^n \tag{2.5}$$

where λ, β and n are the free parameters and R_g is the geometrical major radius of a device, and the plasma boundary determined by

$$\begin{aligned} R &= R_0 + a\cos\left(\theta + \delta\sin\theta\right) \\ Z &= Z_0 + \kappa a\sin\theta \end{aligned} \tag{2.6}$$

where R_0 and Z_0 are the radial and vertical plasma position, a is the minor radius, κ and δ are the elongation and the triangularity respectively, and θ is the geometrical poloidal angle. Then the VFIT is run using the generated sensor signals as inputs. The reconstructed flux and current distribution is in a perfect match with the exact solution as shown in Figure 2.6. The shape parameters of the exact solution are $R_0 = 0.4$ m, $Z_0 = 0.0$ m, $a = 0.3$ m, $\kappa = 2.0$, and $\delta = 0.8$, which are typical in VEST. All sensor signals are fit to less than 1%. The convergence is achieved after 20 iterations.

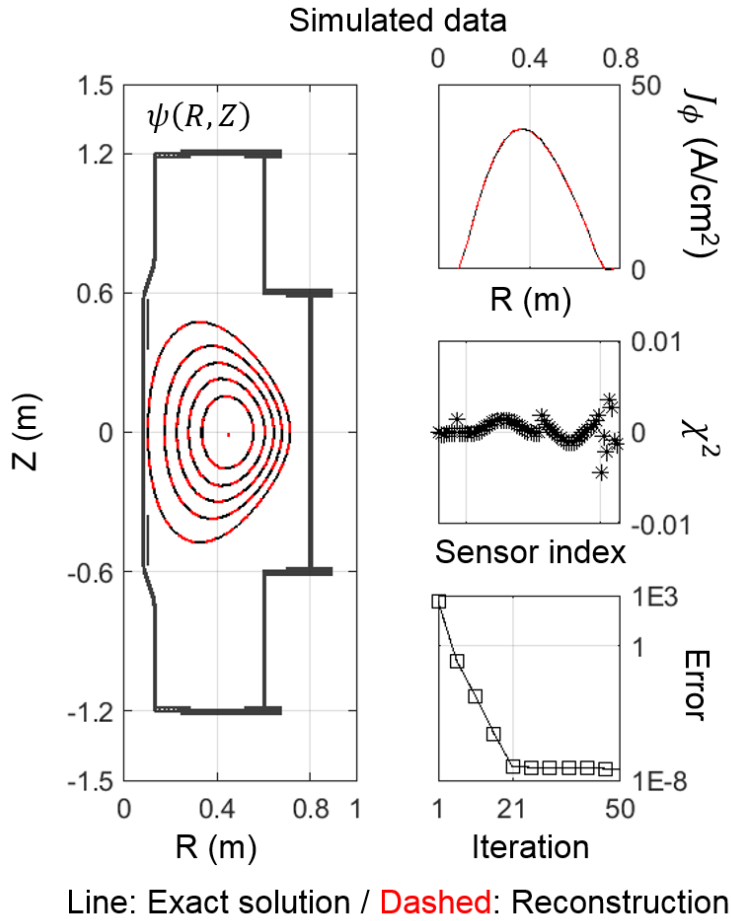

Figure 2.6 VFIT run result from the simulated data. The shape parameters of the exact solution are $R_0 = 0.4$ m, $Z_0 = 0.0$ m, $a = 0.3$ m, $\kappa = 2.0$, and $\delta = 0.8$, which are typical in VEST. All sensor signals are fit to less than 1%. The convergence is achieved after 20 iterations.

Real data includes noise and signal that need to be separated carefully. The real magnetic diagnostics sensor signals are from: the plasma current (signal), the plasma current outside the last closed flux surface, the PF coil current, and the wall current induced by both plasma and PF coil currents. The PF coil current is easily measured, and then its contribution to the magnetic diagnostics sensor signals is computed using the relation $\psi = GI$ where the Green's function

$$G \equiv \frac{\mu_0 u}{2\pi}\left(\left(1-\frac{k^2}{2}\right)K\left(k^2\right)-E\left(k^2\right)\right) \tag{2.7}$$

where K and E are the elliptic integrals of the first and second kind respectively, and

$$\begin{aligned} u^2 &= \left(r+r'\right)^2+\left(z-z'\right)^2 \\ k^2 &= 4rr'/u^2 \end{aligned} \tag{2.8}$$

where (r,z) and (r',z') are the points of evaluation and source. The wall current by the PF coil currents is computed from the measured PF coil currents using the circuit model

$$0 = R_v I_v + M_{vv'}\frac{dI_{v'}}{dt} + M_{vc}\frac{dI_c}{dt} \tag{2.9}$$

where R and M are the resistance and the inductance, I is the current, and the subscripts v and c denote the vacuum vessel element and the coil element respectively. The vacuum vessel and the coil are discretized by 432 and 530 thin toroidal shell elements respectively [25]. Due to the complex geometry of VEST vacuum vessel, it is impractical to fit the wall currents using the diagnostics data as reported in [26].

The computation of the wall current by the plasma current and the plasma current outside the last closed flux surface require the plasma current distribution as an input. Note that the goal of the equilibrium reconstruction is to find a detailed plasma current distribution, but only a rough estimate is needed here. A set of 12

squared elements are used to model the plasma current distribution [23], and the currents of each elements are used as a coil current equivalent in Equation (2.9) for the computation of the wall current by the plasma current. The plasma boundary can be found by deducing the poloidal flux distribution from the currents of each elements and determining the plasma boundary through comparison of the poloidal flux at the limiter and x-points [24], and the current outside the found boundary is then the plasma current outside the last closed flux surface. For a more accurate evaluation of the plasma current outside the last closed flux surface, a recently developed modified Cauchy condition surface method [27] may replace the method described in this paragraph.

VFIT run result from the real data of shot #18452, at 0.306 s is shown in Figure 2.7. The profile parameters are empirically set at $n_p = 3$ and $n_F = 2$. The hollow current density profile with a higher peak at the inboard side is typical in the fast current ramp up of a spherical torus. The sensor signals are fit to 10% on average. The convergence is achieved after 64 iterations. The convergence criteria is set to 10^{-3} to meet the input condition of the fixed boundary equilibrium solvers and stability codes.

Useful equilibrium parameters can be post-processed from the reconstructed equilibrium flux surfaces. The coordinate conversion from real (R,Z) to flux surface (ψ_N,θ) is achieved by the field line following, i.e., angle marching along a field line (along each ψ_N surface)

$$\begin{aligned} dR &= R\frac{B_R}{B_\phi}d\theta \\ dZ &= R\frac{B_Z}{B_\phi}d\theta \end{aligned} \tag{2.10}$$

starting from the points on the line connecting the magnetic axis and the outboard midplane. The line searching method [28] is unstable, presumably because of the

strong shaping of VEST plasmas. When the (R,Z) of each (ψ_N,θ) grid is computed using Equation (2.10), the plasma shape and profile parameters can be computed. One example is the safety factor, which is computed using

$$q(\psi_N > 0.15) = \oint \frac{F}{R^2 B_\theta} dl \tag{2.11}$$

where $F = RB_\phi$ is evaluated from integrating the reconstructed FF' function, B_θ is deduced from the ψ distribution, and the number 0.15 is selected empirically. A singularity occurs when Equation (2.11) is used near the magnetic axis, so the approximate relation [24]

$$q_0 \approx \frac{F_0}{R_0}\left[\det H(\psi_0)\right]^{-1/2} \tag{2.12}$$

is used for the on-axis safety factor and the remaining parts are found by Modified Akima cubic Hermite interpolation. In Equation (2.12), the subscript 0 denotes the magnetic axis and H is the Hessian matrix related to the derivative of the poloidal flux, evaluated near the magnetic axis.

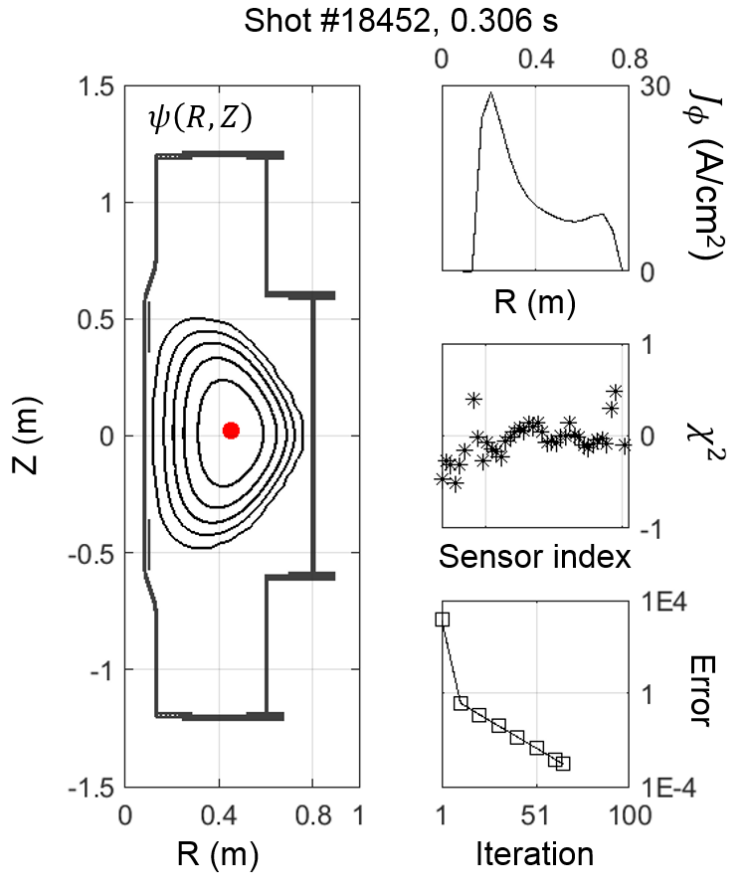

Figure 2.7 VFIT run result from the real data of shot #18452, at 0.306 s. The profile parameters are $n_p = 3$ and $n_F = 2$. The hollow current density profile with a higher peak at the inboard side is typical in the fast current ramp up of a spherical torus. The sensor signals are fit to 10% on average. The convergence is achieved after 64 iterations. The red dot indicates the magnetic axis.

2.2.2. Mode identification

Mode information of a magnetic fluctuation – the toroidal (n) and poloidal (m) mode numbers, the amplitude and the frequency – bears the characteristics of the instability. A general method to determine the mode information from a set of Mirnov coils involves a Fourier analysis and a singular value decomposition [29].

Toroidal array of 2 Mirnov coils is placed 30° apart at the outboard sections K and J (see Figure 2.5). A raw data from the toroidal array is shown in Figure 2.8. Considering a Fourier transform $X(\omega)$ of a measured signal dB_Z/dt, the cross spectrum of the toroidal array

$$C_{12}(\omega) = \left\langle X_1(\omega) X_2^*(\omega) \right\rangle_{\Delta\omega} \tag{2.13}$$

can be used to compute the coherence or cross power from the amplitude

$$P_{12}(\omega) = \left[C_{12}(\omega) C_{12}^*(\omega) \right]^{1/2} \tag{2.14}$$

and the phase angle from the phase difference

$$\Delta\phi_{12}(\omega) = \tan^{-1}\left[\mathrm{Im}\{C_{12}(\omega)\} / \mathrm{Re}\{C_{12}(\omega)\} \right] \tag{2.15}$$

where $\langle\ \rangle_{\Delta\omega}$ in Equation (2.13) is the average over a small frequency $\Delta\omega$. Then, the mode frequency f is determined from the peaks in the cross power spectrum, and the toroidal mode number n is determined by

$$n = \Delta\phi_{12} / \Delta\phi_{coils} \tag{2.16}$$

where $\Delta\phi_{coils}$ is the geometrical angle between the Mirnov coils (30°).

Poloidal array of 25 Mirnov coils is placed at the inboard section b and outboard section J (see Figure 2.5). The toroidal angle between the inboard and outboard coils (105°) is synchronized by digital phase shifting based on discrete Fourier transition, assuming there is no poloidal rotation within the short analysis time interval. Also, the signals are band pass filtered at the mode frequency by a digital, finite impulse

response (FIR) band pass filter with the order of 250 and using the Hamming window for smoothing. Considering a data matrix

$$M = \frac{1}{\sqrt{pq}} \begin{pmatrix} b_1(t_1) & \cdots & b_q(t_1) \\ \vdots & \ddots & \vdots \\ b_1(t_p) & \cdots & b_q(t_p) \end{pmatrix} \tag{2.17}$$

where b is the digitized signal and the subscripts p and q denote the number of samples and sensors respectively, the information on the correlation of each columns can be extracted from the singular value decomposition

$$M = USV^T \tag{2.18}$$

where U and V are matrices composed of the phase angle eigenvectors on temporal and spatial correlation respectively and S is the diagonal matrix with the coherence eigenvalues as entries [30]. The data matrix is scaled with the root sum squared for the stability of the decomposition [31]. The poloidal mode number m is determined from a phase angle diagram of the dominant spatial correlation eigenvectors, as shown in Figure 2.8.

The mode identification is performed every 0.2 ms, within 1 ms (i.e., ±0.5 ms) time window. First, the toroidal mode number and frequency are determined, then the poloidal array signals are filtered at the mode frequency, and the poloidal mode number is determined. The modes of each time slices with the same toroidal mode number are put together to formulate a mode following analysis as shown in Figure 2.9. The mode amplitude of each modes is computed by weighting the relative correlation of each modes on the signal from a Mirnov coil located at the outboard midplane.

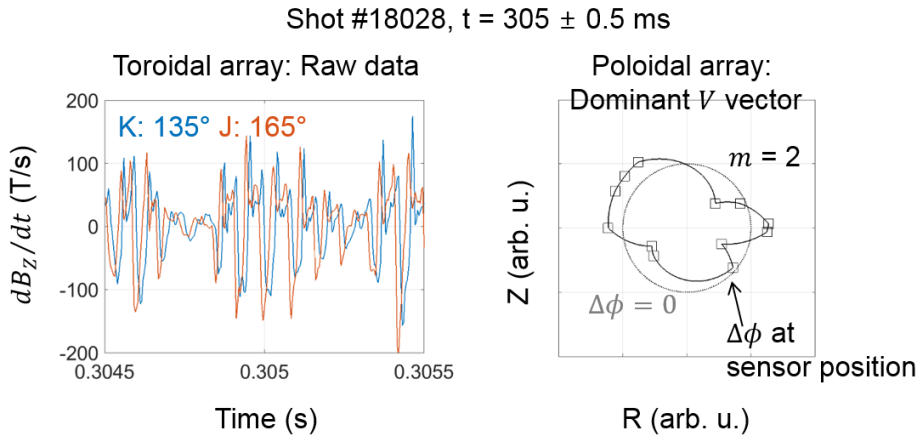

Figure 2.8 Raw data of the toroidal array of 2 Mirnov coils and phase angle diagram of the dominant spatial correlation eigenvector of shot #18028, within 0.305 ± 0.0005 s.

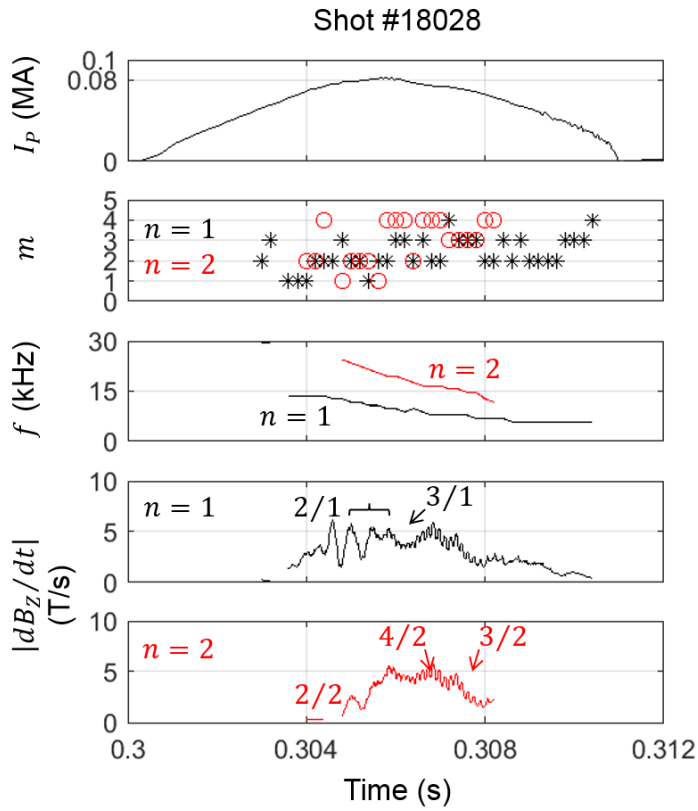

Figure 2.9 Mode following analysis of shot #18028. The color represents each modes and the circles and asterisks denote the poloidal mode number. The mode numbers are overlaid on the mode amplitudes: The mode amplitude of each modes is computed by weighting the relative correlation of each modes on the signal from a Mirnov coil located at the outboard midplane.

2.3. Internal magnetic probes

Internal magnetic probes provide the useful direct measurements when the perturbation to the plasma is small. The insulating materials reportedly absorb the plasma energy [13], causing the plasma temperature and hence the plasma current to decrease. In VEST, however, the plasma current decrease with the internal magnetic probes is no more than 10% [14], presumably because of the small plasma size and energy.

The location of the internal magnetic probes are shown in Figure 2.10 and Figure 2.11. Total 8 sensor groups cover $R > 0.30$ m with the spatial resolution $\Delta R = 0.05$ m on midplane. A sensor group is composed of a Hall sensor (previously used in e.g. [32]) and two chip inductors (previously used in e.g. [33]), with the Hall sensor directed to measure the equilibrium B_ϕ and the chip inductors directed to measure both equilibrium and fluctuating B_Z and B_R. The enclosure sets the cutoff frequency for the chip inductors at 41 kHz, lower than the self-resonant frequency at 90 MHz, while the Hall sensor response is limited to 23 kHz. The specifications of the sensors used in the internal magnetic probe array are summarized in Table 2.3. Note that at Hall sensors can measure dc, whereas chip inductor signals at dc is zero. A schematic of a sensor group in the internal magnetic probe array is shown in Figure 2.12. Note the directions of two chip inductors.

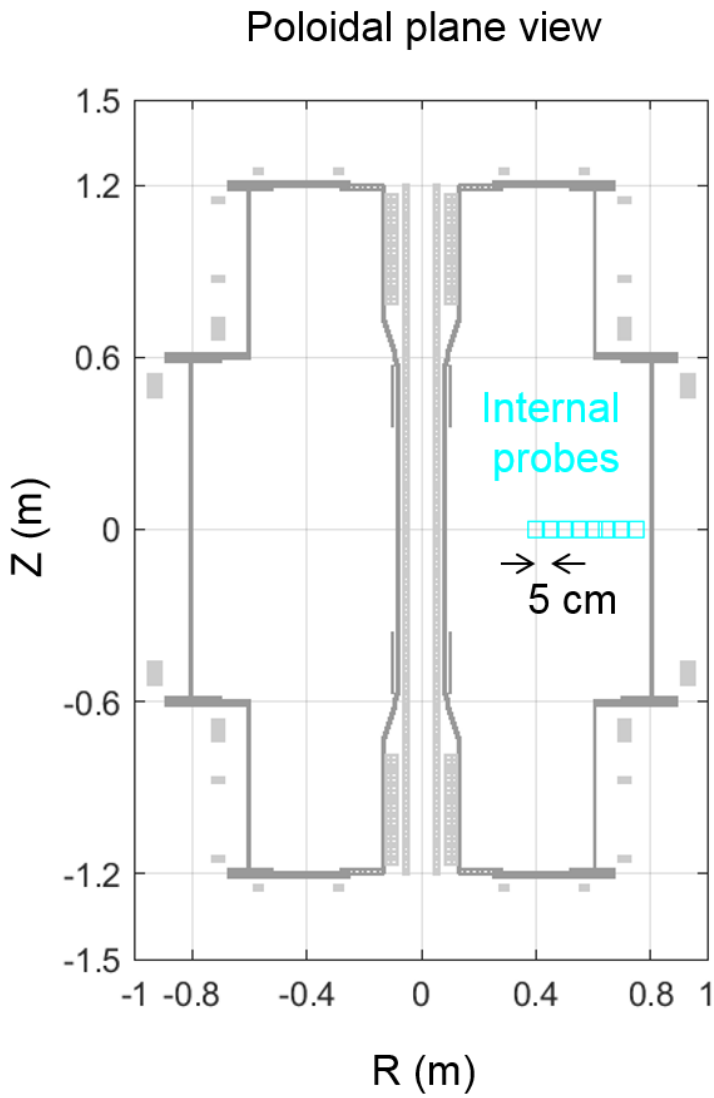

Figure 2.10 Location of the internal magnetic diagnostics sensors: Poloidal plane view. Internal magnetic probe locations are colored in cyan.

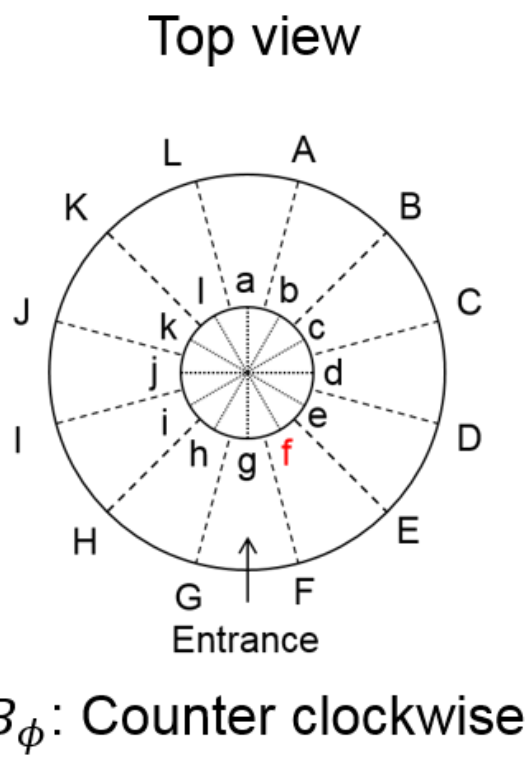

Figure 2.11 Location of the external magnetic diagnostics sensors: Top view. The highlighted sections f is where the internal magnetic diagnostics sensors are located.

Table 2.3 Specifications of the sensors used in the internal magnetic probe array. See Figure 2.12 for the arrangement of the sensors within a sensor group. The chip inductor gain is the effective area, computed from the inductance value and the sensor dimensions. The chip inductor frequency response is limited by the self-resonant frequency. Note that at Hall sensors can measure dc, whereas chip inductor signals at dc is zero.

	Hall sensor	Chip inductor
Model (Manufacturer)	WSH315-XPCN2 (Winson)	1008CS-472XJLB (Coilcraft)
Gain	1.5 mV/G ± 20%	1 cm^2 (52 turns)
Frequency response	0 – 23 kHz	< 90 MHz
Dimension	3.1×3.0×1.2 mm	2.9×2.8×2.0 mm
Remark		Inductance: 4.7 μH ± 5%

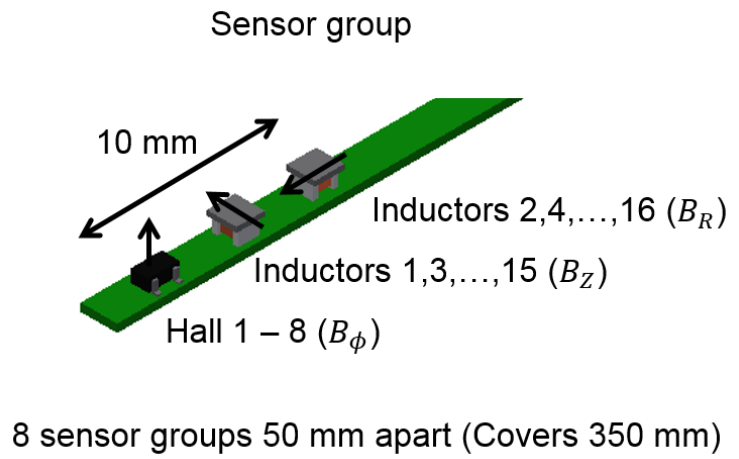

Figure 2.12 Schematic of a sensor group in the internal magnetic probe array. The sensors are indexed starting from the innermost sensors. Note the directions of two chip inductors.

Mount of the internal magnetic probes is provided by a printed circuit board (suggested in [34], followed by [35]) with the form factor of 3.6×500 mm and the thickness of 0.8 mm, on which the probes are scattered within 10 mm (see Figure 2.12). All probes are machine soldered by surface mount technology (SMT) for an accurate alignment. The Hall sensor power grid is embedded in the printed circuit board, forming a network of 8 parallel connected Hall sensors. The twisted pair of 0.1 mm litz wires are soldered manually to each sensors as the signal lines.

Enclosure for the internal magnetic probes is shown in Figure 2.13 and Figure 2.14. The probes are placed at the air side, and the vacuum boundary is held at the 1/4 inch stainless steel pipe and the quick disconnect. The 1/2 inch stainless steel pipe is used to fit the 1/4 inch pipe inside the flexible bellows. The cylindrical structure at the rear end provides the electromagnetic shield against the noise pickup. The probes can be moved between shots using the flexible bellows assisted by a linear guide (not shown in the figures). The stainless steel pipes provide the electrostatic insulation, and the 10 mm outer diameter alumina tube provides the thermal insulation. The insertion of the enclosure causes up to 10% plasma current decrease [14].

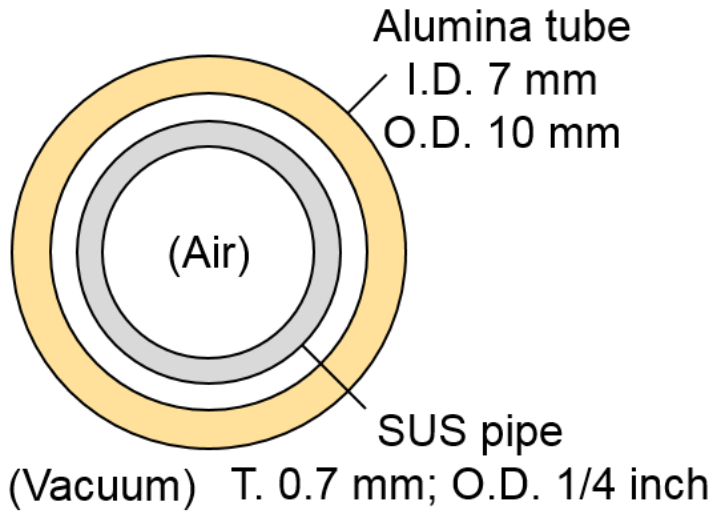

Figure 2.13 Enclosure for the internal magnetic probes: Nose view. The probes are placed at the air side, and the vacuum boundary is held at the 1/4 inch stainless steel pipe and the quick disconnect (see Figure 2.14).

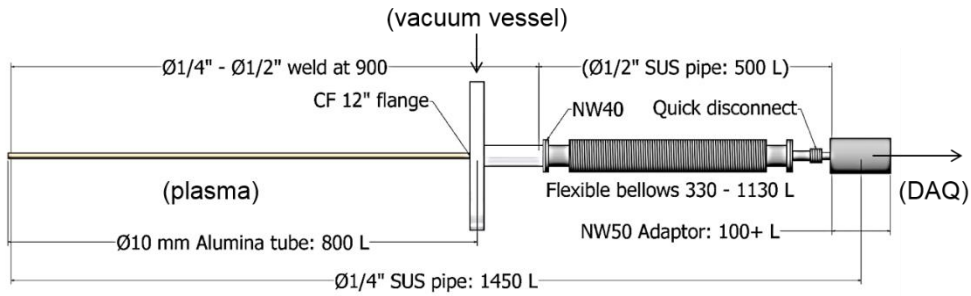

Figure 2.14 Enclosure for the internal magnetic probes: Side view. The vacuum boundary is held at the 1/4 inch stainless steel pipe (see Figure 2.13) and the quick disconnect. The 1/2 inch stainless steel pipe is used to fit the 1/4 inch pipe inside the flexible bellows. The cylindrical structure at the rear end provides the electromagnetic shield against the noise pickup. The probes can be moved between shots using the flexible bellows assisted by a linear guide (not shown).

Calibration of the internal magnetic probes includes three steps. First, a Helmholtz coil with 14 turns and 3 cm radius, powered by the AFG3000C function generator (Tektronix) coupled with the EP-4000 audio amplifier (Beringher) to provide the sinusoidal current waveforms of amplitudes up to 10 A at 20 – 20 kHz for several seconds, is used for the bench calibration [36]. Then, the misalignment is computed using the conversion matrix [14]

$$\begin{pmatrix} \tilde{B}_\phi \\ \tilde{B}_Z \end{pmatrix} = \begin{pmatrix} \cos\theta & -\sin\theta \\ \sin\theta & \cos\theta \end{pmatrix} \begin{pmatrix} B_\phi \\ B_Z \end{pmatrix} \tag{2.19}$$

where tilde denotes the measured fields, no tilde denotes the real fields, and θ is the misaligned angle, as shown in Figure 2.15. Note that the toroidal and vertical field measurements are assumed to be perfectly perpendicular, taking into account that the probes are machine soldered. The signals before and after the misalignment calibration is shown in Figure 2.16 (a), in the inset of which the separation of the B_Z pickup in the B_ϕ probe is highlighted. Next, the measured toroidal fields are cross referenced with the expected toroidal field computed using the probe position and the $1/R$ dependency of the toroidal field in a tokamak as shown in Figure 2.16 (b). The assumed probe positions are also compared to the positions predicted based on the measurement upon installation of the probes. After the calibrations, the probes are moved 5 cm in or out to check the signal reproduction of the overlapping probes.

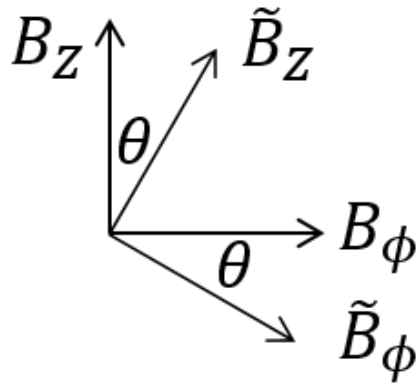

Figure 2.15 Schematic for the conversion matrix of Equation (2.19). Note that the toroidal and vertical field measurements are assumed to be perfectly perpendicular, taking into account that the probes are machine soldered.

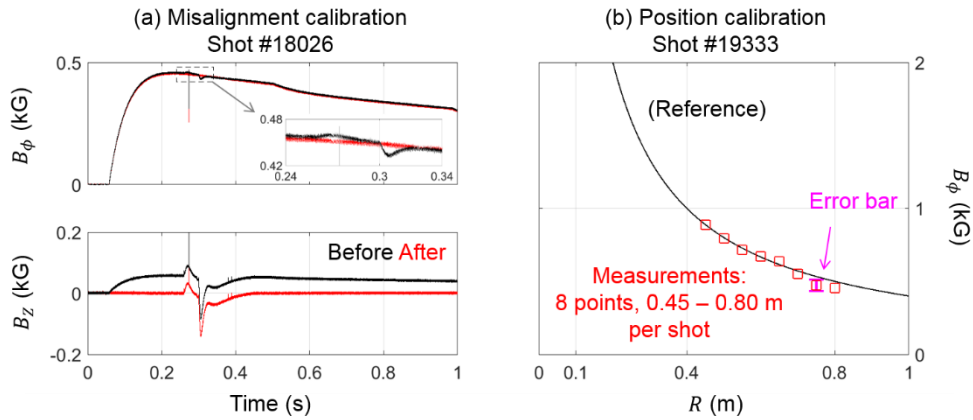

Figure 2.16 Misalignment and position calibration. (a) The signals before (black) and after (red) the misalignment calibration. The inset highlights the separation of the B_Z pickup in the B_ϕ probe. (b) Cross reference of the measured toroidal fields with the expected toroidal field computed using the probe position and the $1/R$ dependency of the toroidal field in a tokamak.

Chapter 3. Internal Structure of Tearing Modes

3.1. Phase reversal layers

Magnetic islands naturally emerge from a tearing mode excitation [5], and takes a physical form of a helical current sheet spiraling on a flux surface where the safety factor corresponds to the mode number by $q = m/n$ [37]. Assuming the width of the current sheet is small compared to the plasma minor radius, the helical current can be modelled by a small toroidal current filament rotating in a poloidal direction, with its own magnetic axis. The schematic of a magnetic island in a tokamak and the predicted characteristic dB_Z/dt structure are shown in Figure 3.1. The magnetic axis of the island shown in the top view rotates in poloidal direction along the trace shown in the side view. The island current distribution shows this is a 2/1 mode island. Assuming the island current comes out of the paper near the sensors, it can be predicted that $B_Z < 0$ at all times at sensor B location. Considering dB_Z/dt, on the other hand, the island is below midplane at time t_1, moving towards the sensors from below, while the island is above midplane at time t_2, moving away from the sensors, generating the characteristic phase reversal structure at the location between sensors A and B where an axis of a magnetic island passes by. Therefore, if an island exists, the phase reversal is measured. When and only when the phase reversal also *behaves* like a magnetic island, the phase reversal measurement can be said to imply the magnetic island existence. The statement that the phase reversal behaves like a magnetic island will be argued through the remainder of this section and further elaborated in Section 3.2.

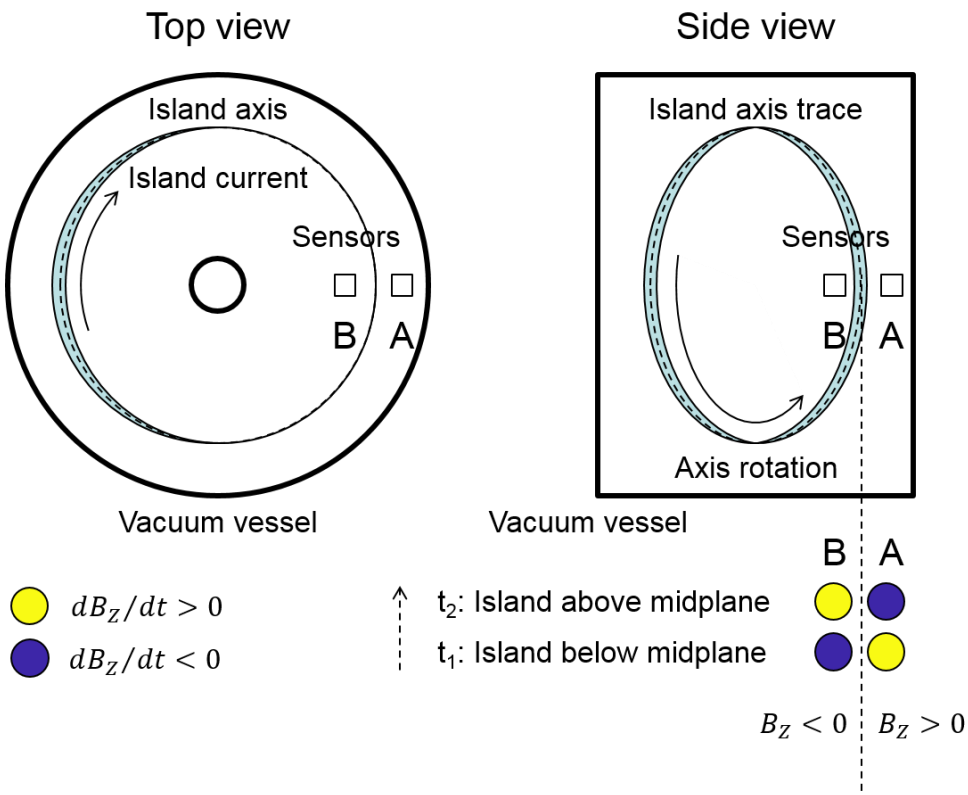

Figure 3.1 Schematic of a magnetic island in a tokamak and predicted characteristic dB_Z/dt structure. The magnetic axis of the island shown in the top view rotates in poloidal direction along the trace shown in the side view. The island current distribution shows this is a 2/1 mode island. Assuming the island current comes out of the paper near the sensors, it can be predicted that $B_Z < 0$ at all times at sensor B location. Considering dB_Z/dt, on the other hand, the island is below midplane at time t_1, moving towards the sensors from below, while the island is above midplane at time t_2, moving away from the sensors, generating the characteristic phase reversal structure at the location between sensors A and B where an axis of a magnetic island passes by.

Internal magnetic probe measurements of the phase reversal structure is shown in Figure 3.2. The contour plot presents the time evolution (abscissa) of the radial profile of $\delta_t B_Z \equiv dB_Z/dt$ along the midplane (ordinate) during 0.308 ± 0.0002 s of both (a) shot #18452 and (b) shot #18457. The overlaid white dashed lines are the locations of $q=2$ and $q=3$ surfaces reconstructed using VFIT, near which the phase reversal occurs. When the probes are inserted further inside, only the inner ($q=2$) phase reversal structure is captured, whereas when the edge region is also covered by the probes, both inner and edge ($q=3$) phase reversal structure are captured. Another observation is that 3-4 periodic phase reversal structures are captured within 0.4 ms time window, which is around 10 kHz in frequency. Considering that the Mirnov coil picks up the mode frequency

$$f = nf_{rot,plasma} \tag{3.1}$$

where $f_{rot.plasma}$ is the rotation frequency of the plasma, the plasmas shown in Figure 1.3 and Figure 2.9 also rotate at around 10 kHz, matching the frequency of the phase reversal structure occurrence. In summary, the phase reversal structure is (a) located near rational flux surfaces and (b) periodic with the frequency matching the Mirnov coil measurement results, supporting the statement that the phase reversal behaves like a magnetic island, which will be further elaborated in Section 3.2.

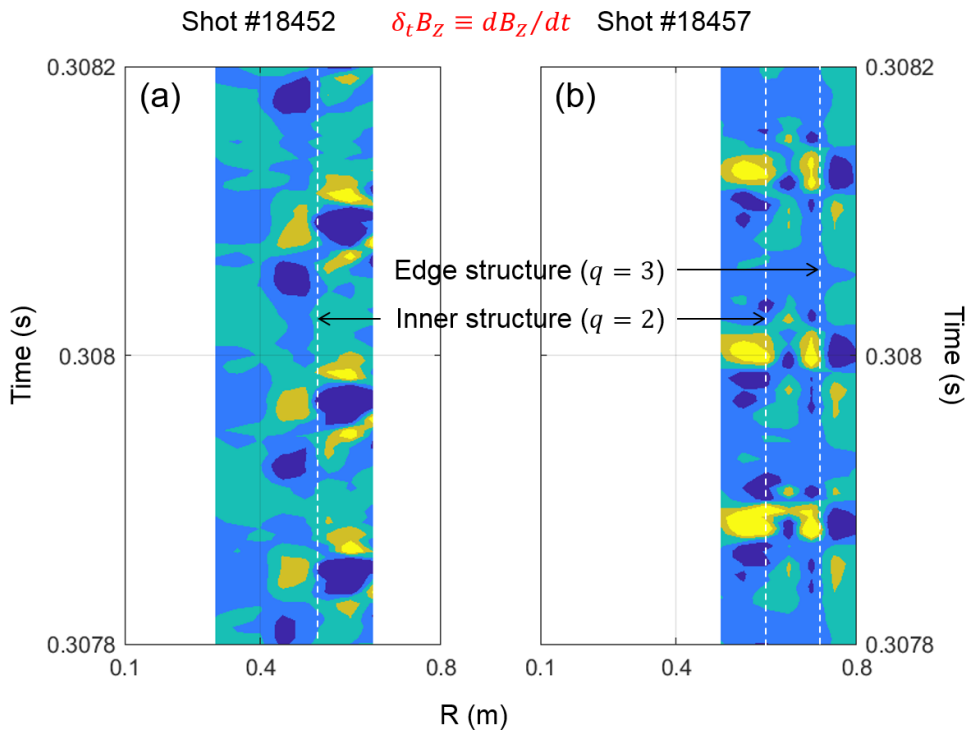

Figure 3.2 Internal magnetic probe measurements of the phase reversal structure. The contour plot presents the time evolution (abscissa) of the radial profile of $\delta_t B_Z \equiv dB_Z/dt$ along the midplane (ordinate) during 0.308 ± 0.0002 s of both (a) shot #18452 and (b) shot #18457. See lower left corner of Figure 3.1 for the coloring convention. The overlaid white dashed lines are the locations of $q = 2$ and $q = 3$ surfaces reconstructed using VFIT.

3.2. Phase reversal and island chain location

Phase reversal and island chain location measured using the internal and external magnetic diagnostics are shown in Figure 3.3. The identical shots from #18452 to #18457 are repeated while the internal magnetic probes are progressively retracted from $R > 0.30$ m (#18452) to $R > 0.50$ m (#18457)[1] with the step size of 0.05 m. The signals from each shot are averaged, i.e. accumulated and divided by the number of overlapping measurements, for a wider coverage than that of a single shot. The time evolution of the magnetic axis, $q = 2$ and $q = 3$ surfaces reconstructed using VFIT are overlaid (white lines) on the contour plot of the magnetic fluctuation amplitude $|dB_Z/dt|$ for comparison in Figure 3.3 (a). Note the peak of $|dB_Z/dt|$ is naturally located at the phase reversal (see Figure 3.1). Two distinct $|dB_Z/dt|$ peaks are observed near the $q = 2$ and $q = 3$ surfaces during 0.306 – 0.310 s, when first the 2/1 + 3/2 and then the 3/1 + 4/2 modes are identified as shown in Figure 3.3 (c), (e) and (f). Safety factor of shots shown in Figure 3.3 is shown in Figure 3.4. The magenta error bar shows the uncertainty in computation of $q_{\min.}$ near the magnetic axis (See Section 2.2.1, near Equation (2.11) for more details), which explains the absence of the $q = 1.5$ surface when a 3/2 mode exists at 0.306 s, as shown in Figure 3.3. In summary, the mode numbers correspond to the helicity of the phase reversal bearing flux surface, strongly supporting the statement that the phase reversal behaves like a magnetic island. Then the logic dictates the phase reversal measurement implies the magnetic island existence. Moreover, that an island structure is measured using the internal magnetic probes conclusively shows that the instability during a tokamak current ramp up is a tearing mode.

[1] Shot #18454 failed due to human error (PEV closed – no prefill gas injection).

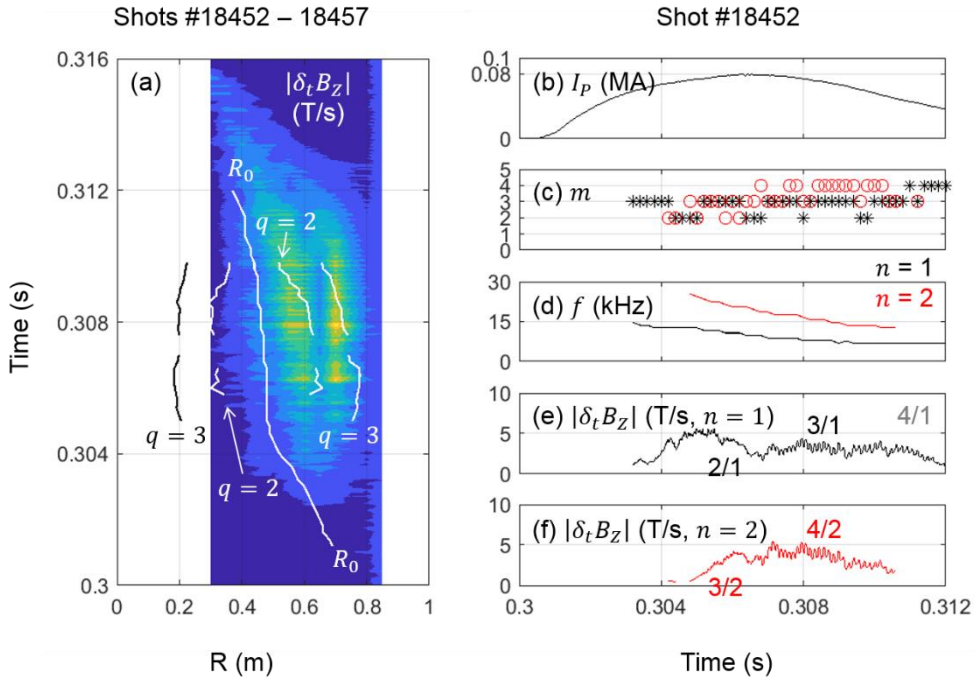

Figure 3.3 Phase reversal and island chain location measured using the internal and external magnetic diagnostics. (a) The time evolution (abscissa) of the radial profile of average $|dB_Z/dt|$ along the midplane (ordinate) during the identical shots from #18452 to #18457, with the overlaid time evolution of the magnetic axis, $q = 2$ and $q = 3$ surfaces (white lines) reconstructed using VFIT. (b) Plasma current. (c-f) Mode characteristics (see Figure 2.9).

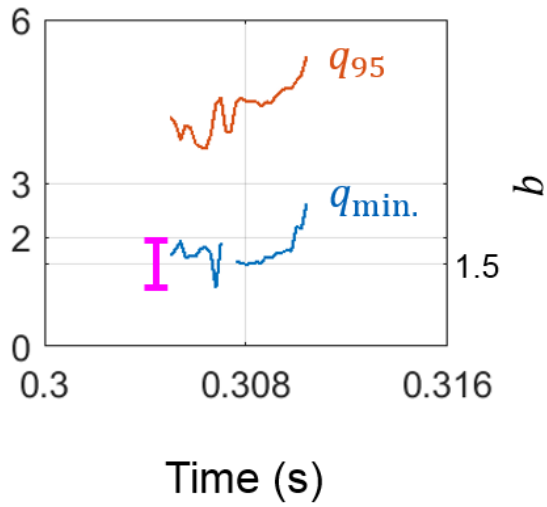

Figure 3.4 Safety factor of shots shown in Figure 3.3. The magenta error bar shows the uncertainty in computation of $q_{\min.}$ near the magnetic axis (See Section 2.2.1, near Equation (2.11) for more details), which explains the absence of the $q = 1.5$ surface when a 3/2 mode exists at 0.306 s, as shown in Figure 3.3.

3.3. Dynamics of island chains

Phase reversal measurement is both necessary and sufficient for the magnetic island existence as argued through Section 3.1 and 3.2. Then, the dynamics of the magnetic islands can be studied using the internal magnetic probes.

Time evolution of the magnetic islands during shot #18455 is shown in Figure 3.5. Two magnetic islands are onset simultaneously, are phase locked to each other, and move to the inboard with the bulk plasma. Note that the frequency of the periodic phase reversal structure occurrence is dropping with time, in agreement with the data from the Mirnov coil signal shown in Figure 3.3 (d).

The magnetic islands moving together as they are phase locked is intriguing, since the previous understandings were that the adjacent island would merge and become an island large enough to even cause a disruption [38] or at least compete until only the stronger island remains [39]. Instead, Figure 3.5 shows that the magnetic islands are in-phase and move together for several resistive diffusion times ($\tau_\eta \sim 3$ ms in VEST). Note that the seemingly merged magnetic islands in Figure 3.5 (c) is actually two magnetic islands blurred together due to the limited spatial resolution of the measurement (indicated as the red error bar to be 5 cm) considering that in Figure 3.5 (d) two islands are seen again which implies that either the magnetic islands are merged then separated, or they are more likely not merged at all.

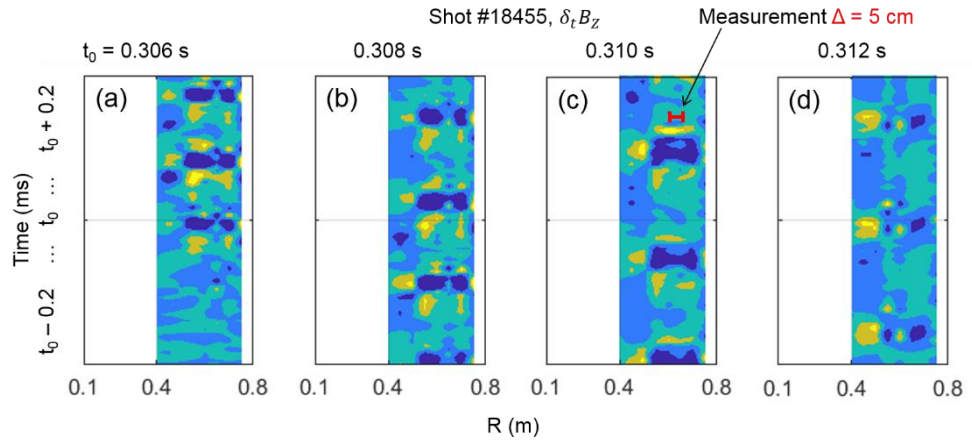

Figure 3.5 Time evolution of the magnetic islands during shot #18455. See lower left corner of Figure 3.1 for the coloring convention and Figure 3.2 for the axis information. (a) Two magnetic islands are onset simultaneously, (b-c) are phase locked to each other, and (d) move to the inboard with the bulk plasma. The red error bar is the measurement resolution of 5 cm.

3.4. Island width identification by Mirnov coils

Island width and its growth rate have been the primary subjects of modelling in the study of both classical [40] and neoclassical [41] tearing modes. The magnetic island width is generally related to the external Mirnov coil signals with the calibration factor determined from a direct measurement of the island [11], using the relation

$$w = C\left(\frac{16}{n}\frac{L_q R_0}{B_{\phi 0}}\left|\frac{dB_R}{dt}\right|\right)^{1/2} \tag{3.2}$$

where C is the calibration factor, n is the toroidal mode number, $L_q \equiv q/(dq/dr)$ is the radial gradient scale length of the safety factor profile, $B_{\phi 0}$ is the toroidal magnetic field at the major radius R_0, and dB_R/dt is the radial magnetic field fluctuation

$$\left|\frac{dB_R}{dt}\right| = \frac{1}{2}\left(\frac{R_w - R_0}{r}\right)^{m+1}\left|\frac{dB_Z}{dt}\right| \tag{3.3}$$

where R_w is the outboard midplane radius, r is the minor radius of the resonant flux surface, m is the poloidal mode number, and dB_Z/dt is the vertical magnetic field fluctuation at the outboard midplane. The calibration factor C is most commonly determined by the electron cyclotron emission (ECE) radiometry, but an internal magnetic probe measurement is used here (see Section 1.1 for the reason) as shown in Figure 3.6. The equilibrium parameters are summarized in the inset table. The outboard midplane Mirnov coil signal weighted by the relative correlation of $n = 2$ mode is shown in the lower left corner, beside the contour plot of the internal magnetic probe measurements of dB_Z/dt. The island width is estimated to be 10-15

cm at the time when the Mirnov coil signal amplitude is 60 T/s, resulting in the calibration factor $C = (1.1 - 1.7) \times 10^{-3}$.

Implication of the calibration factor C determination is that the island width can be estimated from the external Mirnov coil signal when the internal magnetic probes are removed.

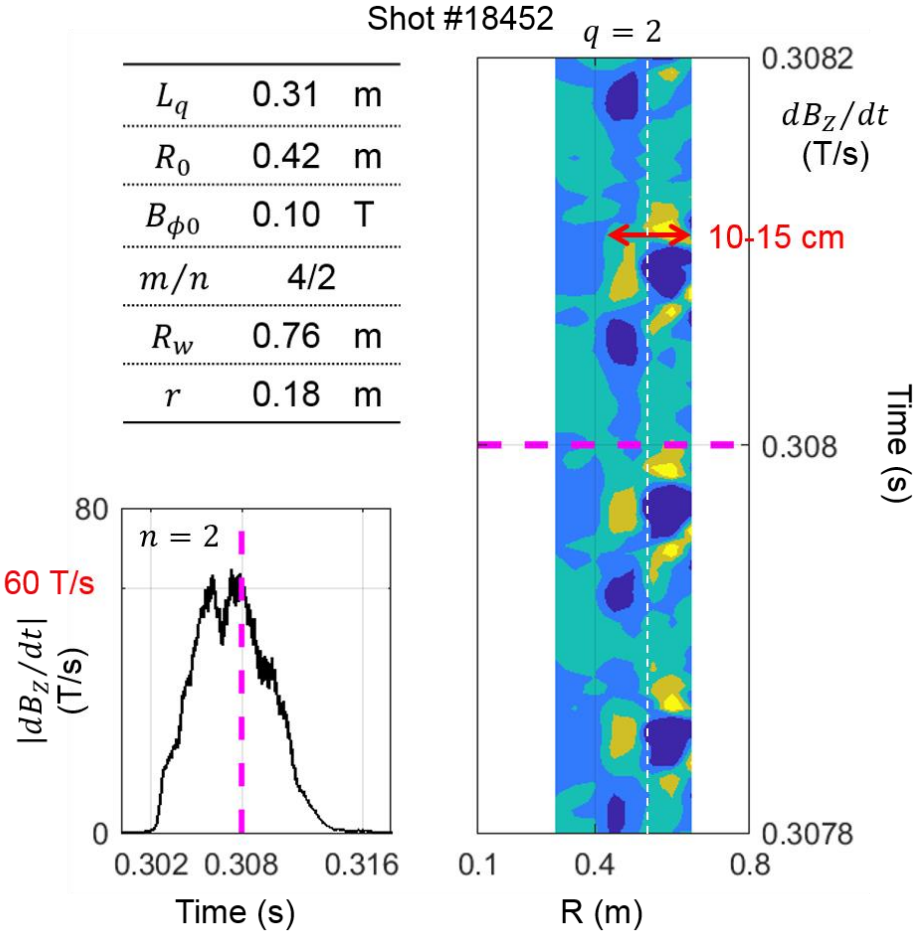

Figure 3.6 Determination of the island width calibration factor by the internal magnetic probes, using data of shot #18452, at 0.308 s. The equilibrium parameters reconstructed using VFIT are summarized in the inset table. The outboard midplane Mirnov coil signal weighted by the relative correlation of $n = 2$ mode is shown in the lower left corner, beside the contour plot of the internal magnetic probe measurements of dB_Z/dt. See Figure 3.2 for the axis information. The island width is estimated to be 10-15 cm at the time when the Mirnov coil signal amplitude is 60 T/s, resulting in the calibration factor $C = (1.1-1.7)\times 10^{-3}$.

Chapter 4. Tearing Mode Response to Operation Variables

Chapter 3 established that the instability during a tokamak current ramp up is a tearing mode. General methods to control the tearing mode in a tokamak are the current ramp rate [8], prefill gas pressure [9], plasma shape [10], and wall condition [4]. The test of the current ramp rate (Section 4.1 and Section 4.2) and the prefill gas pressure (Section 4.3) control knobs are presented in Chapter 4. The other control knobs are left to be tested in the future, when the plasma shape control capability is improved through e.g. the H-bridge PF coil power supply [42], or the in-situ wall condition diagnostic capability is improved through e.g. MAPP (materials analysis particle probe) [43].

4.1. Current ramp rate

Experiment on the tearing mode response to the current ramp rate control is shown in Figure 4.1, as the prefill gas pressure, plasma current, outboard midplane Mirnov coil signal amplitude with the mode numbers, plasma shape factor [10] involving the elongation and triangularity reconstructed using VFIT, and ratio of the OI (777 nm) and Hα (656 nm) line emissions measured using the filterscopes [44]. Note that the plasma relevant time marked as grey dashed lines in (a) is expanded in (b-e). The line emission ratio shown in (e) is reportedly proportional to the surface oxygen content which characterizes the wall condition [45].

In Figure 4.1, as the plasma current ramp rate is increased in shot #18653 (red lines) with reference to shot #19101 (black lines) by decreasing the C2 capacitance of PF01 to 10 mF (see Section 2.1, Table 2.2), the Mirnov coil signal amplitude is increased. To interpret the result, it is theorized that the faster plasma current ramp rate results in an increased accumulation of the skin current (with a finite time for the current to diffuse in), which implies a more hollow current density profile, a lower average magnetic shear dq/dr, and an increased susceptibility to the classical tearing mode [40]. To test the theory, the safety factor and current density profiles during the current ramp rate control experiment are shown in Figure 4.2. The total currents of the profiles from shot #18653 (red line) and shot #19101 (black line) are comparable at 80 kA. With reference to shot #19101, the current density profile is broader in shot #18653 as expected from the faster current ramp rate, resulting in the lower average magnetic shear as theorized. In summary, the classical tearing mode theory explains the response of the tearing mode to the current ramp rate control.

Control of the variables prefill gas pressure and wall condition is acceptable but the plasma shape factor is larger in shot #18653 than in shot #19101. However, the

plasma shape factor reportedly stabilizes the instability during a tokamak plasma current ramp up, though not supported by a model [10]. Therefore, the increased Mirnov coil signal amplitude in shot #18653 may be attributed to the faster current ramp rate with reference to shot #19101, but not to the increased shaping, while an additional experiment is designed (see Section 4.2) to further clarify the issue.

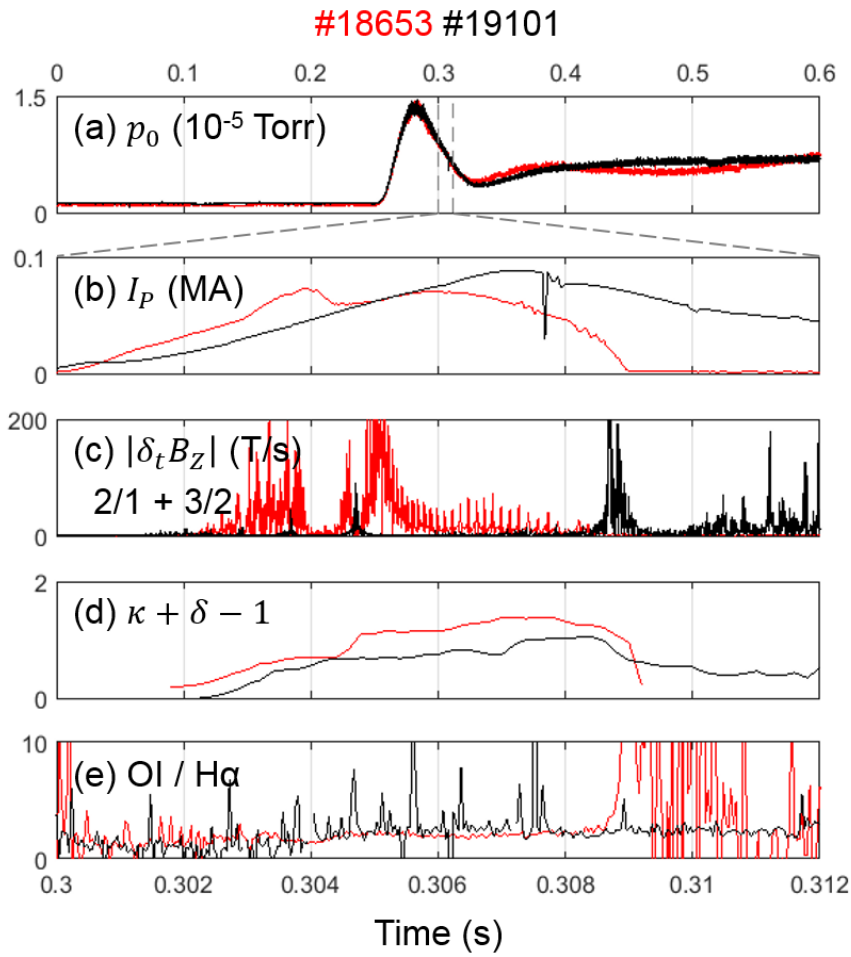

Figure 4.1 Experiment on the tearing mode response to the current ramp rate control, involving shot #18653 (red lines) and shot #19101 (black lines). (a) Prefill gas pressure. (b) Plasma current. (c) Outboard midplane Mirnov coil signal amplitude with the mode numbers overlaid. (d) Plasma shape factor [10] involving elongation and triangularity reconstructed using VFIT. (e) Ratio of the OI (777 nm) and Hα (656 nm) line emissions measured using the filterscopes [44]. Note that the plasma relevant time marked as grey dashed lines in (a) is expanded in (b-e). The line emission ratio shown in (e) is reportedly proportional to the surface oxygen content which characterizes the wall condition [45].

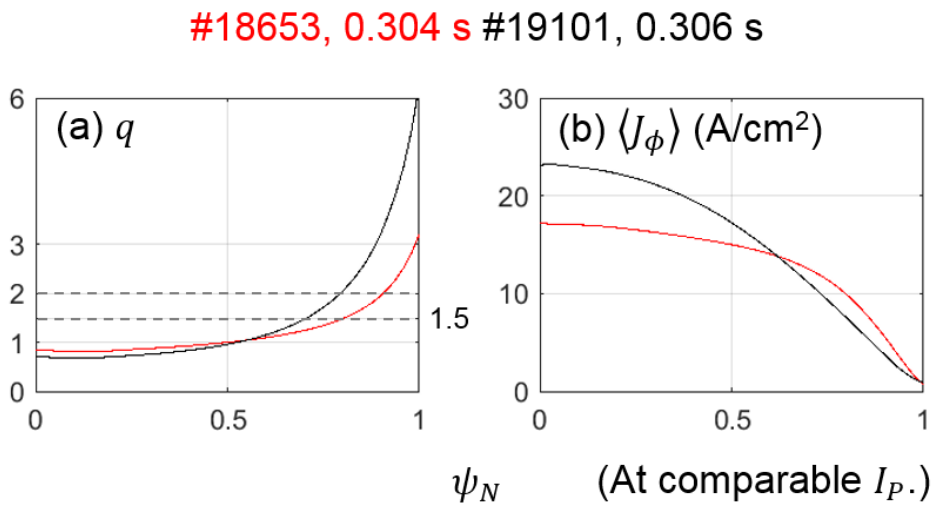

Figure 4.2 Safety factor and current density profiles during the current ramp rate control experiment. The total currents of the profiles from shot #18653 (red line) and shot #19101 (black line) are comparable at 80 kA. The variables are flux averaged and reconstructed using VFIT.

4.2. Local magnetic shear

To further clarify the interpretation of Figure 4.1 based on the classical tearing mode theory, an experiment is designed to control the local magnetic shear itself. The experiment on the tearing mode response to the local magnetic shear control is shown in Figure 4.3, as the on axis vacuum loop voltage computed from the PF coil and wall currents (see Section 2.2.1), plasma current, outboard midplane Mirnov coil signal amplitude of $n=1$ (grey lines) and $n=2$ (black lines) modes with the mode numbers overlaid, and magnetic shears on the $q=3$ (d, grey lines) and $q=2$ (e, black lines) flux surfaces which are followed considering the mode numbers 3/1, 2/1, 4/2 and 3/2 are excited, and the reconstruction of the $q=1.5$ surface is less accurate.

In Figure 4.3, in addition to the sinusoidal loop voltage drive, a second loop voltage drive is produced at 0.305 s by the PF01 C3 switching. Then, the safety factor and current density profiles are perturbed as shown in Figure 4.4. With the second loop voltage drive, the slightly hollow current density profile (blue lines) becomes more hollow (red line), then relaxes back (yellow line), resulting in the evolution of the safety factor profile, i.e. the magnetic shear dq/dr. Prior to the second loop voltage drive, the magnetic shear at $q=3$ surface increases as the 3/1 mode is suppressed. With the second loop voltage drive, the magnetic shear at $q=2$ surface decreases as the 2/1 mode is onset. The onset and suppression of a (m,n) mode coincides with the change in the magnetic shear dq/dr at the $q=m/n$ surface, as predicted by the classical tearing mode theory. This elaborates on the argument of Section 0 that the classical tearing mode theory explains the response of the tearing mode to the current ramp rate control.

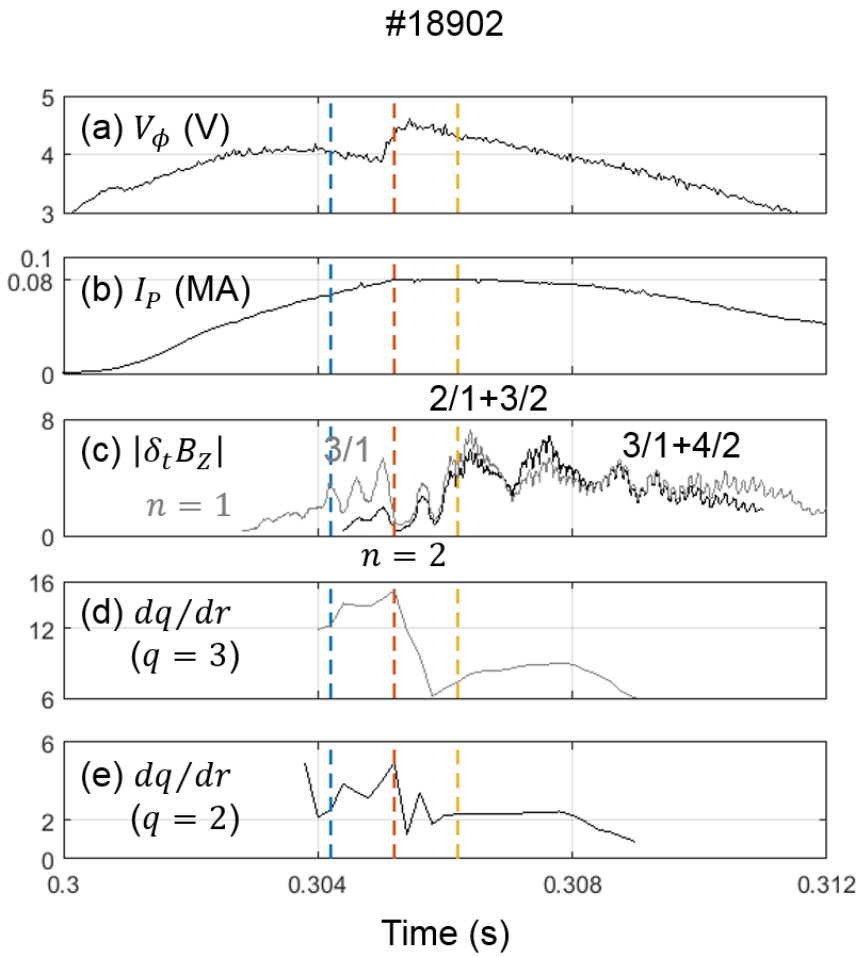

Figure 4.3 Experiment on the tearing mode response to the local magnetic shear control, involving shot #18902. (a) On axis vacuum loop voltage computed from the PF coil and wall currents (see Section 2.2.1). (b) Plasma current. (c) Outboard midplane Mirnov coil signal amplitude of $n=1$ (grey lines) and $n=2$ (black lines) modes with the mode numbers overlaid. (d-e) Magnetic shears on the $q=3$ (d, grey lines) and $q=2$ (e, black lines) flux surfaces. The colored dashed lines correspond to the profiles shown in Figure 4.4.

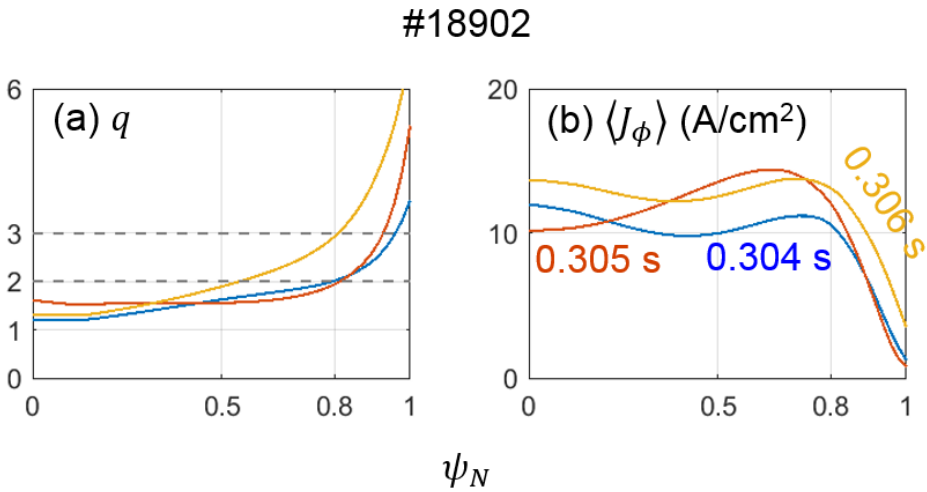

Figure 4.4 Safety factor and current density profiles during the local magnetic shear control experiment. The line colors correspond to the dashed lines in Figure 4.3. The variables are flux averaged and reconstructed using VFIT.

4.3. Prefill gas pressure

Experiment on the tearing mode response to the prefill gas pressure is shown in Figure 4.5, as the same variables as in Figure 4.1. As the prefill gas pressure is increased in shot #18731 (red lines) with reference to shot #19157 (black lines) by increasing the PEV open time, the Mirnov coil signal amplitude is increased. To interpret the result, the same theorization as in Section 0 is devised: The higher prefill gas pressure results in a lower plasma temperature, a higher plasma resistivity, and a faster current penetration, which implies a more peaked current density profile, a higher average magnetic shear dq/dr, and an increased stability to the classical tearing mode [40]. However, it is apparent that the tearing mode becomes more unstable with the increased prefill gas pressure. Although the classical tearing mode theory explained the tearing mode response to the current ramp rate control, the theory fails to explain the tearing mode response to the prefill gas pressure control. In the safety factor and current density profiles shown in Figure 4.6, the current density profile is more peaked in shot #18653 with reference to shot #19101 as expected from the failed theorization. In summary, the average magnetic shear dq/dr increases with the higher prefill gas pressure as expected, but the tearing mode unexpectedly becomes more unstable. Therefore, an alternative to the classical tearing mode theory is needed to explain the response of the tearing mode to the prefill gas pressure control. Section 4.4 elaborates on this statement.

Control of the variables plasma current ramp rate and plasma shaping factor is acceptable but the wall condition is better (the surface oxygen content is lower [45]) in shot #18731 with reference to shot #19157, which may have resulted in a higher edge current density in Figure 4.6 (b) but does not harm the overall theorization.

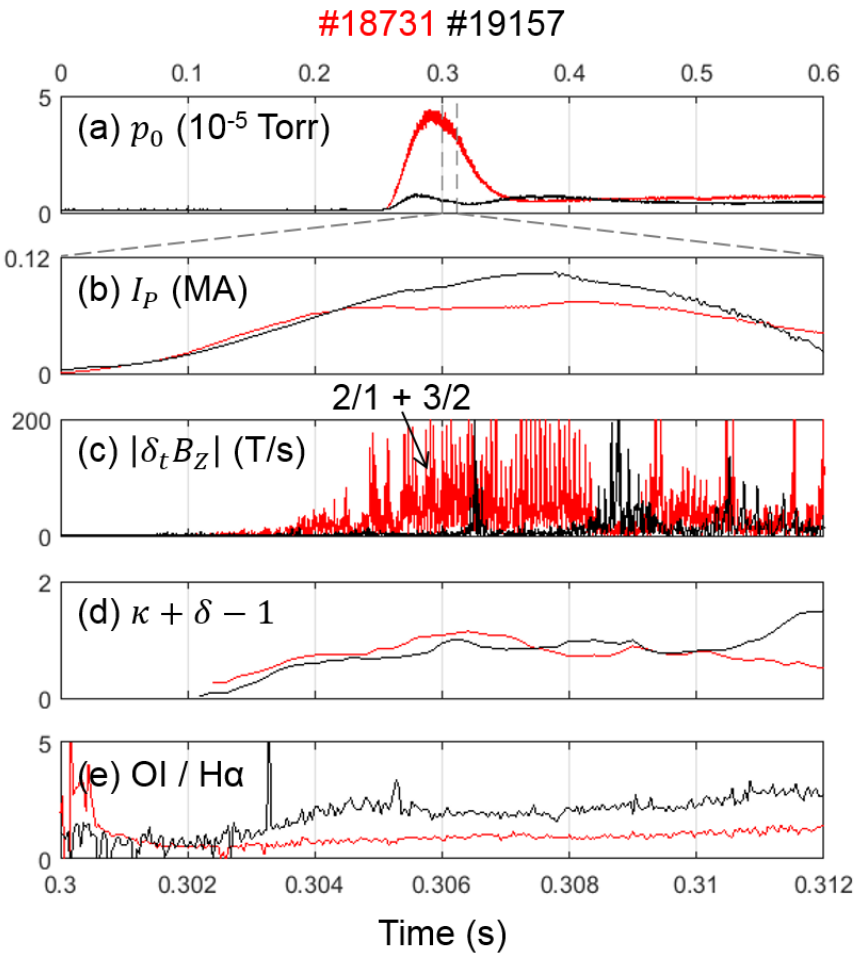

Figure 4.5 Experiment on the tearing mode response to the prefill gas pressure involving shot #18731 (red lines) and shot #19157 (black lines). See Figure 4.1 for the description.

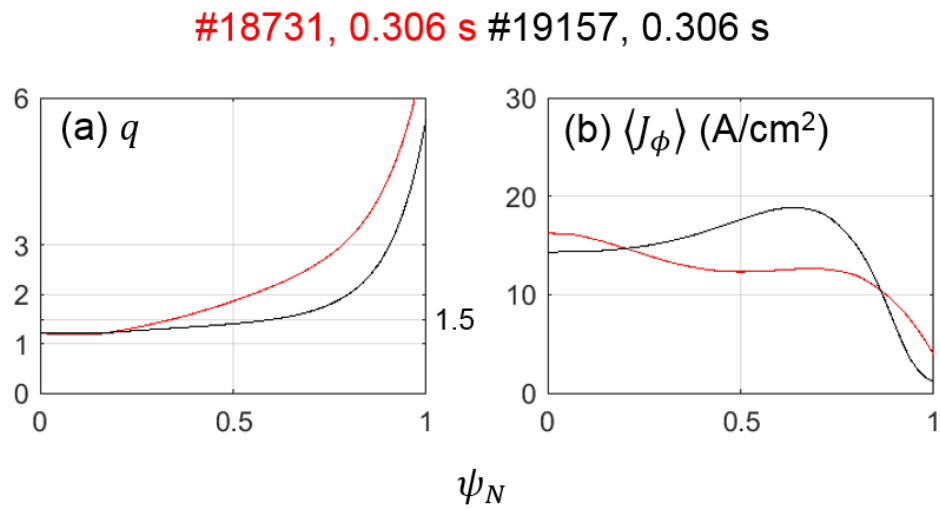

Figure 4.6 Safety factor and current density profiles during the prefill gas pressure control experiment. The variables are flux averaged and reconstructed using VFIT.

4.4. Interpretation of tearing mode control

Normalized magnetic fluctuation is plotted against the current ramp rate and the prefill gas pressure for the database of 71 shots from March to April 2018 with the maximum plasma currents over 70 kA as shown in Figure 4.7. The normalized magnetic fluctuation naturally characterizes the tearing mode activity, and the correlation of variables can be quantified by the Pearson correlation coefficient

$$\rho_{AB} = \frac{\mathrm{cov}(A, B)}{\sigma_A \sigma_B} \tag{4.1}$$

where σ is the standard deviation and cov is the covariance. Comparing the Pearson correlation coefficients, the prefill gas pressure is a control knob as effective as the current ramp rate for the tearing mode control. Therefore, a unified theory is needed to explain the response of the tearing mode to the prefill gas pressure control as well as the current ramp rate control.

Prefill gas pressure was assumed to work on the tearing mode control indirectly by affecting the current density profile [9]. However, Figure 4.6 shows that the safety factor and current density profile during the prefill gas pressure control do not explain the increased Mirnov coil signal amplitude. In fact, this contradiction has been previously reported [46] but the suggested interpretation by the thermal instability theory [47] was also inconclusive. On the other hand, a spherical torus such as VEST is predicted [48] and proved [49] to be more stable to high plasma beta, allowing for the existence of a bootstrap current even at the early phase of the operation. Therefore, it is presumed that in VEST, the neoclassical tearing mode theory [41] may explain the response of the tearing mode during a plasma current ramp up to the control knobs of current ramp rate and prefill gas pressure.

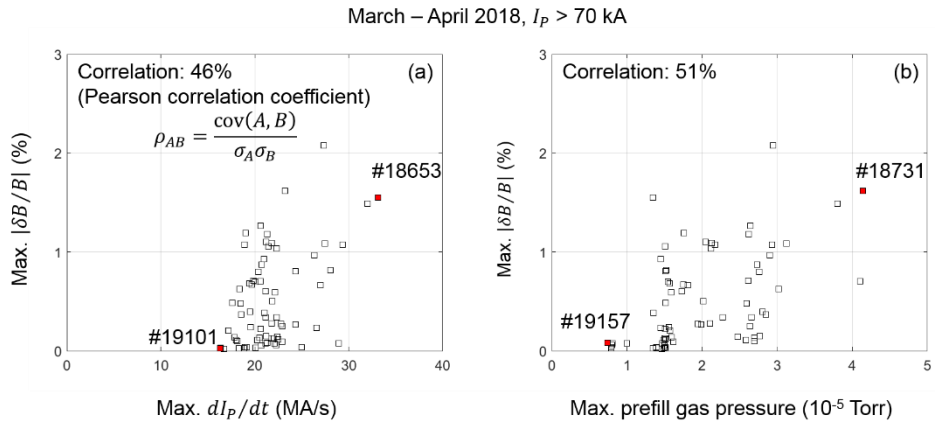

Figure 4.7 Plot of normalized magnetic fluctuation against (a) the current ramp rate and (b) the prefill gas pressure for the database of 71 shots from March to April 2018 with the maximum plasma currents over 70 kA. The normalized magnetic fluctuation naturally characterizes the tearing mode activity, and the correlation of variables is quantified by the Pearson correlation coefficient.

Chapter 5. Discussion

Chapter 4 established that the tearing mode during a tokamak current ramp up is not explained using the classical tearing mode theory, and presumed that the neoclassical tearing mode theory may provide the explanation. In general, the magnetic island width evolution is modelled using the modified Rutherford equation [7] as will be presented in Section 5.1. Moreover, the interpretation of the fluctuation asymmetry requires the neoclassical tearing mode existence as will be presented in Section 5.2. Building on the arguments in Section 5.1 and Section 5.2, the operational means suggested to avoid the neoclassical tearing mode during the plasma current ramp up will be presented in Section 5.3.

5.1. Modified Rutherford equation modelling

Island width evolution is in general modelled by the modified Rutherford equation

$$1.22^{-1}\frac{\tau_\eta}{r^2}\frac{dw}{dt}=\Delta'+C_R\frac{D_R}{w}+C_B\varepsilon_B^{1/2}\frac{L_q}{L_p}\beta_\theta\left(\frac{1}{w}-\frac{w_{small}^2}{w^3}\right) \tag{5.1}$$

where τ_η, r and w are the plasma resistivity, minor radius at the resonant flux surface and island width respectively, Δ' is the classical tearing mode stability index, $D_R\approx-\left(q^2-1\right)\left(L_q^2/rL_p\right)\beta_\phi$ is the resistive interchange mode stability index where $L_q\equiv q/\left(dq/dr\right)$ and $L_p\equiv-p/\left(dp/dr\right)$ are the radial gradient scale length of the safety factor and pressure profile, and $\varepsilon_B\equiv\left(B_{in}-B_{out}\right)/\left(B_{in}+B_{out}\right)$, β_θ and w_{small} are the magnetic field variation of the inverse aspect ratio, poloidal field and small island effect factor respectively. C_R and C_B are free parameters. In the right hand side, the first term is the classical drive [40], the second term is the curvature stabilization [50], and the last term is the bootstrap current drive [41] with a modification to incorporate the low aspect ratio equilibria [51]. Note that in NSTX [51] and VEST (shot #18731), $\varepsilon_B\approx0.84\varepsilon$ where $\varepsilon\equiv r/R_0$ and R_0 is the major radius.

VFIT (Section 2.2.1) and PEST-3 [52] are used to compute the variables in Equation (5.1): τ_η, r, ε_B, L_q, L_p and β_θ are reconstructed using VFIT, and Δ' and D_R are computed using PEST-3. For the stable run of PEST-3, the fixed boundary equilibrium code CHEASE [53] is used to refine the equilibrium flux surfaces reconstructed using VFIT. For the stable run of CHEASE, which often crashed when the fixed boundary is set at $\psi_N=1.00$, the fixed boundary is set at $\psi_N=0.92$. The error bar in the outputs of PEST-3 due to the plasma boundary

limitation in CHEASE is expected to be less than 10%, based on the comparison of Δ' of a KSTAR discharge computed when the plasma boundary is set at $\psi_N = 1.00$ (red) and $\psi_N = 0.92$ (blue) shown in Figure 5.1. The value of Δ' for 3/2 mode near the magnetic axis is magnified by 10^6 for visualization. The set plasma boundaries are marked with the lines of respective colors on a VEST safety factor profile of shot #18731, at 0.306 s for comparison.

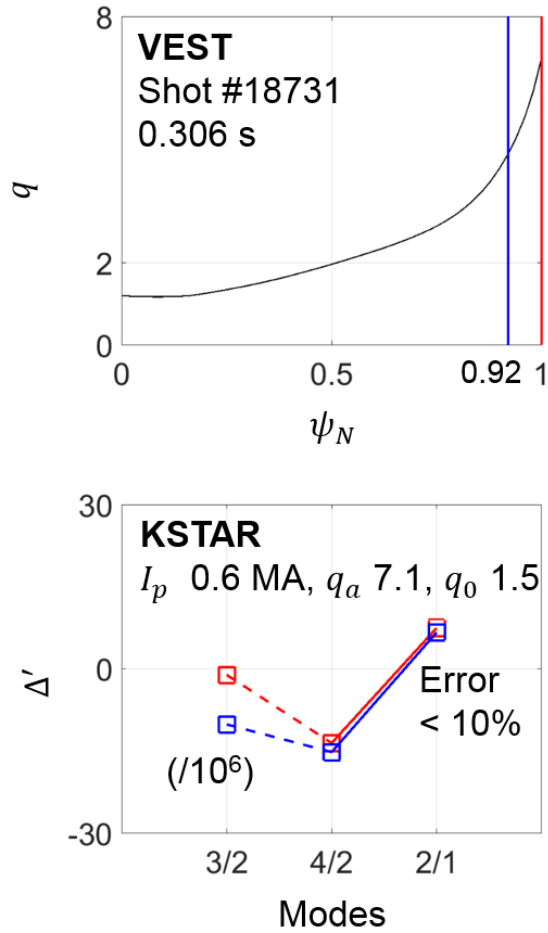

Figure 5.1 Comparison of Δ' of a KSTAR discharge computed when the plasma boundary is set at $\psi_N = 1.00$ (red) and $\psi_N = 0.92$ (blue). The value of Δ' for 3/2 mode near the magnetic axis is magnified by 10^6 for visualization. The set plasma boundaries are marked with the lines of respective colors on a VEST safety factor profile of shot #18731, at 0.306 s for comparison.

Modified Rutherford equation modelling of shot #18731 (high prefill gas pressure case, red lines in Figure 4.5) is shown in Figure 5.2, as the plasma current, outboard midplane Mirnov coil signal amplitude with the mode numbers overlaid, magnetic island width from the measurement using the Mirnov signal (black, see Section 3.4) and the modelling (red), and bootstrap current drive term and Δ' at the $q = 2$ surface. The 2/1 mode island width evolution is followed during 0.3050 – 0.3066 s, assuming a constant small island effect factor $w_{small} = 6\,\text{cm}$. In a high collisionality plasma, the small island effect depends less on the transport threshold factor [54], leading to the relation $w_{small} \approx w_{pol}$ where the ion polarization current factor is

$$w_{pol} \approx \left(3L_q / L_p\right)^{1/2} \varepsilon_B^{-3/4} w_{bi} \tag{5.2}$$

where the ion banana width $w_{bi} = \sqrt{\varepsilon}\rho_{\theta i}$ where the ion poloidal gyroradius is

$$\rho_{\theta i} = \frac{\sqrt{2m_i T_i}}{eB_\theta} \tag{5.3}$$

where m_i and T_i are the ion mass and temperature respectively, e is the elementary charge, and $B_\theta \approx \mu_0 I_p / 2\pi a\kappa$ is the approximate poloidal magnetic field. Assuming $T_i = 10\,\text{eV}$ based on the passive spectroscopy of the intrinsic CIII (464.7 nm) line emission and using the equilibrium variables reconstructed using VFIT, the computed ion banana width $w_{bi} \approx 1\,\text{cm}$ and $\left(3L_q / L_p\right)^{1/2} \varepsilon_B^{-3/4} = (6-8)$.

Modelled and measured 2/1 mode island width evolution are in good agreement during 0.3050 – 0.3066 s before the profiles are redistributed as the second loop voltage drive takes effect. Note the discontinuity in Δ' at 0.3066 s. Apparently, the classical drive is negative while the bootstrap current drive is positive during 0.3050 – 0.3066 s, suggesting a neoclassical tearing mode existence. The seed island may be from the classical tearing mode [55], considering that $\Delta' > 0$ at the onset of the

instability (0.3050 s). The high normalized beta $\beta_N > 2$ and inverse aspect ratio $\varepsilon \sim 0.6$ in VEST, which is a common feature of a low aspect ratio tokamak [56], implies a strong bootstrap current drive, supporting the neoclassical tearing mode existence.

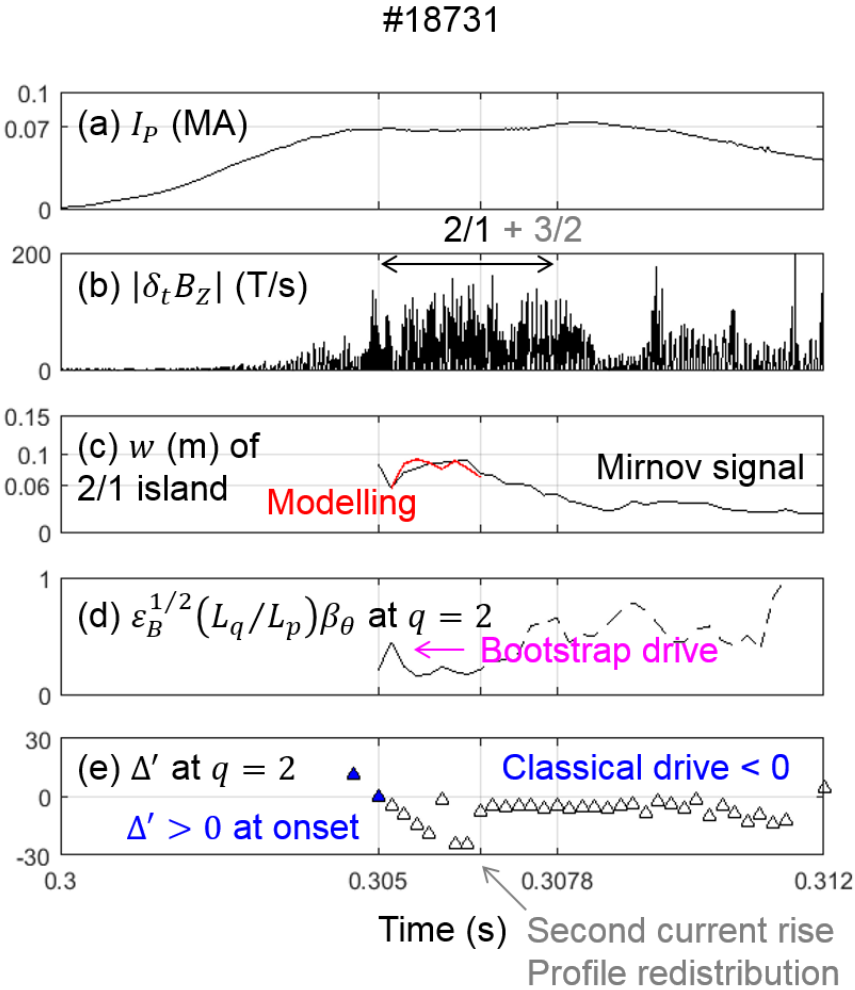

Figure 5.2 Modified Rutherford equation modelling of #18731 (high prefill gas pressure case, red lines in Figure 4.5). (a) Plasma current. (b) Outboard midplane Mirnov coil signal amplitude with the mode numbers overlaid. (c) Magnetic island width: Measurement using the Mirnov signal (black) and modelling (red). (d) Bootstrap current drive term at $q = 2$ surface. (e) Δ' at $q = 2$ surface.

5.2. Fluctuation asymmetry

Two magnetic islands are observed in VEST shots with little exception, at first the 2/1 + 3/2 and then the 3/1 + 4/2 modes (see e.g. Figure 3.3). The theory of the coupled magnetic islands [57] suggests that a (m,n) mode can toroidally couple to a $(m+1,n)$ mode linearly or to a $(2m-1,2n)$ mode nonlinearly. Then, the initial coupling between the 2/1 and 3/2 modes can be explained by the nonlinear toroidal coupling, while the progression of the 2/1 and 3/2 modes into the 3/1 and 4/2 modes can be explained by the linear toroidal coupling. The *nonlinear* coupling implies the involvement of the perturbed bootstrap current, as for the neoclassical tearing modes [57]. Therefore, the specific mode number combination of the coexisting magnetic islands in VEST supports the neoclassical tearing mode existence.

Theory of the coupled magnetic islands [57] also suggests that the nonlinear toroidal coupled magnetic islands can align in phase at the outboard midplane and inverse phase at the inboard midplane. Then, the apparent phase locking of the magnetic islands as shown in Figure 3.5 can be explained by the phase alignment of the 2/1 (3/1) and 3/2 (4/2) nonlinear toroidal coupled magnetic islands. The phase alignment has also been reported in the ECE radiometry of DIII-D [58] and KSTAR [59] discharges. The schematic of the phase aligned nonlinear toroidal coupled magnetic islands is shown in Figure 5.3. The $m=4$ (cyan) and $m=3$ (magenta) magnetic islands are marked with the O and X points along the midplane. The topology of the O and X points suggest that using the wave analogy, a destructive interference will occur at the inboard and a constructive interference will occur at the outboard. Therefore, the observation of the fluctuation asymmetry would support the existence of two magnetic islands by the neoclassical tearing mode excitation.

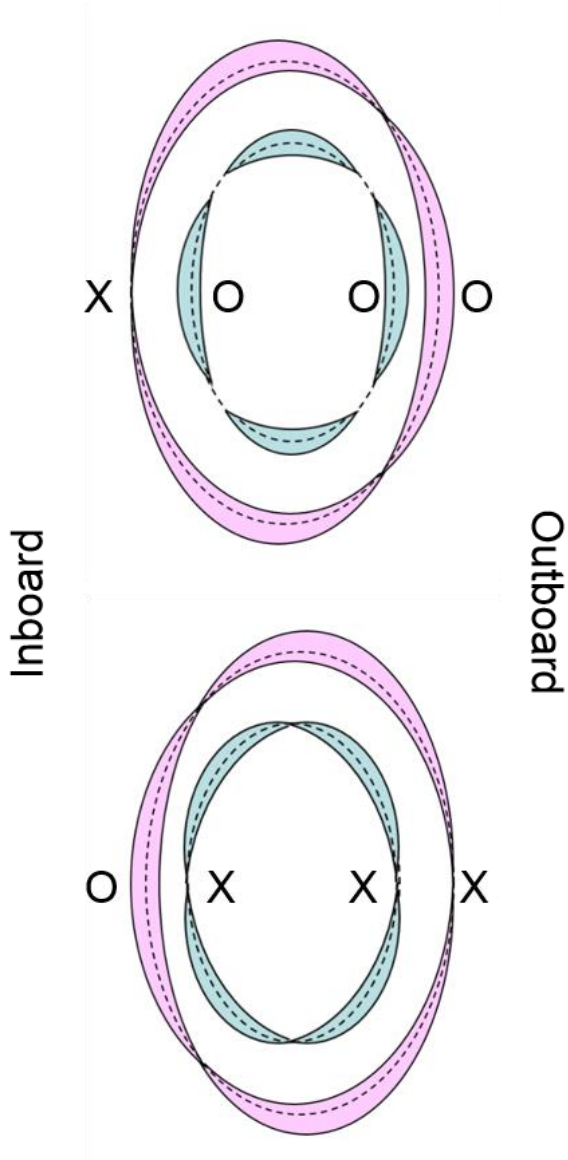

Figure 5.3 Schematic of the phase aligned nonlinear toroidal coupled magnetic islands. The $m = 4$ (cyan) and $m = 3$ (magenta) magnetic islands are marked with the O and X points along the midplane.

Internal magnetic probe measurement of shot #18452 is shown in Figure 5.4, while the magnetic fluctuation profile at 0.308 s of shot #18452 is shown in Figure 5.5, where the abscissa is the geometrical radius from 0.1 to 0.8 m with the locations of the relevant resonant magnetic flux surfaces and magnetic axis marked. The amplitude of the magnetic fluctuation $|dB_Z/dt|$ is smaller at the inboard side of the magnetic axis, by approximately 10 fold on the $q=2$ surface. The outboard Mirnov coil signals are plotted against the outboard Mirnov coil signals for the database of 71 shots from March to April 2018 with the maximum plasma currents over 70 kA as shown in Figure 5.6, indicating that the fluctuation asymmetry is also observed in the external Mirnov coils.

Fluctuation asymmetry has been previously reported in TFTR [60] and ASDEX [61], where the amplitude ratio between the inboard and outboard Mirnov coils ranged from 5 to 20. The validity of the observations was unclear however since there were no internal measurements to confirm the fluctuation asymmetry as shown in e.g. Figure 5.5. Moreover, the physics of the relative phase between the magnetic islands [57] was also unclear at the time.

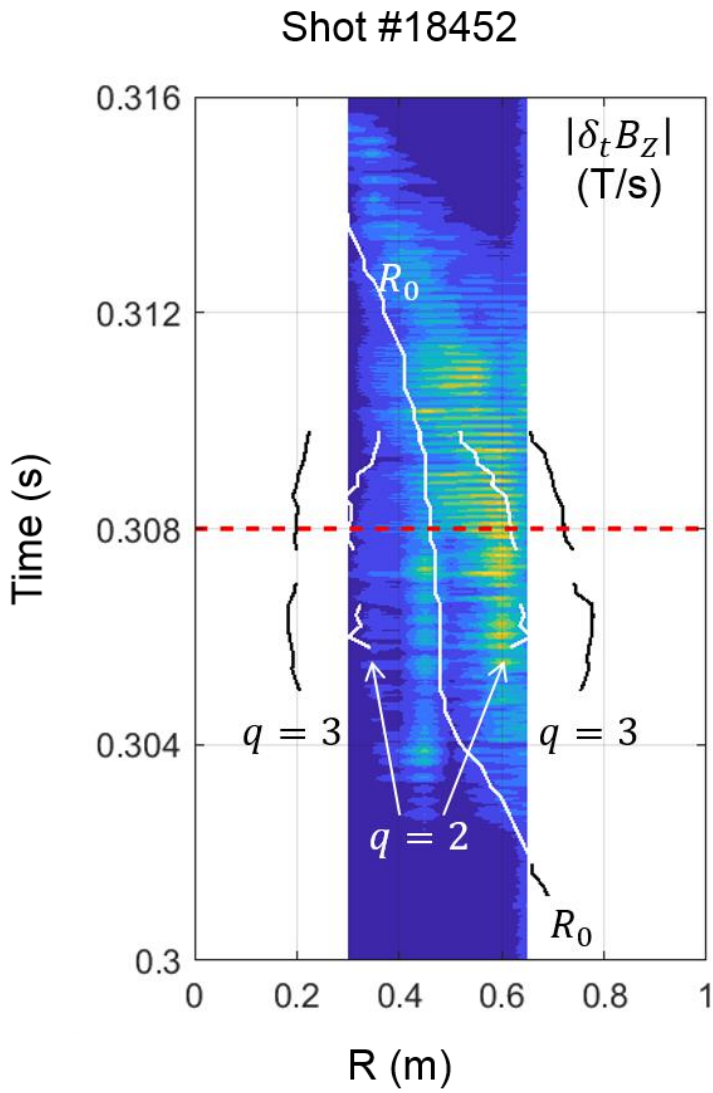

Figure 5.4 Internal magnetic probe measurement of shot #18452. See Figure 3.3 for the contour plot details. The time 0.308 s marked with red dashed line corresponds to the profile shown in Figure 5.5. The amplitude of the magnetic fluctuation $|dB_Z/dt|$ is smaller at the inboard side of the magnetic axis.

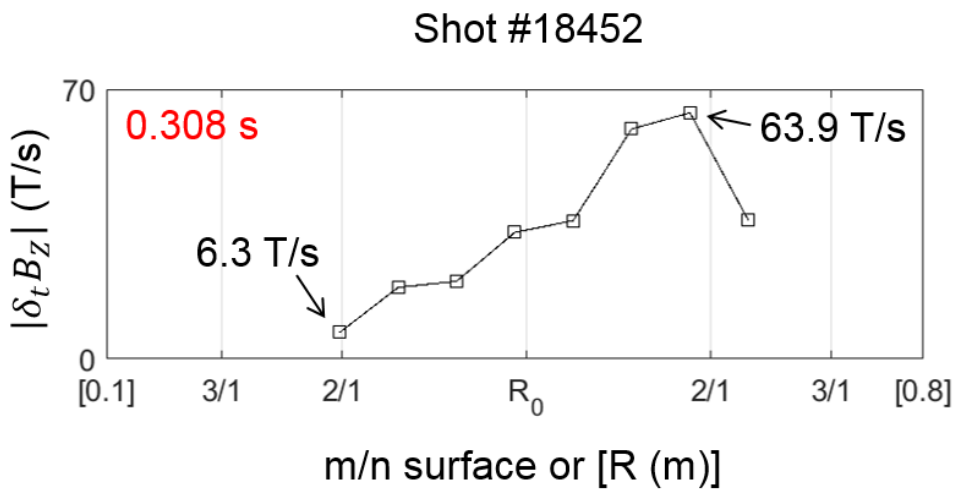

Figure 5.5 Magnetic fluctuation profile at 0.308 s of shot #18452. The time corresponds to the red dashed line shown in Figure 5.4. The abscissa is the geometrical radius from 0.1 to 0.8 m with the locations of the relevant resonant magnetic flux surfaces and magnetic axis marked. The amplitude of the magnetic fluctuation $|dB_Z/dt|$ is smaller at the inboard side of the magnetic axis, by approximately 10 fold on the $q = 2$ surface.

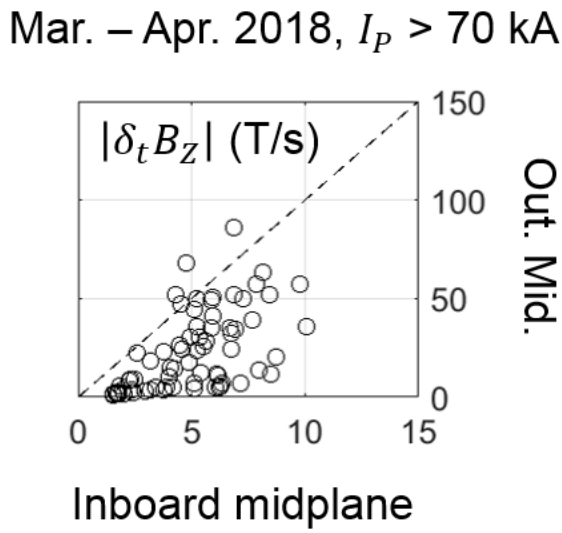

Figure 5.6 Plot of the outboard Mirnov coil signals are plotted against the outboard Mirnov coil signals for the database of 71 shots from March to April 2018 with the maximum plasma currents over 70 kA.

Filament model of a magnetic island [62] is in general used for the electron cyclotron wave targeting system in the neoclassical tearing mode control [63], but can be used for the modelling of the fluctuation asymmetry. The filaments are placed along the $q = m/n$ surface on a poloidal plane, with the grid points found by dividing the poloidal plane into groups, finding the points that minimize $\left|\psi_N - \psi_{N,q=m/n}\right|$, and interpolating the points to get the equiangular filament positions. Then, the perturbed current weightings are assigned to the filaments at the poloidal angle θ as

$$\delta I = I_0 \cos\left(m\theta + \varphi\right) \tag{5.4}$$

where $\varphi = -n\phi + \omega t$ is the relative phase at fixed toroidal angle and time. To fit the variables I_0 and φ using the Mirnov coil signal, the Green's function G is used as in the relation

$$\frac{dB_Z}{dt} = \frac{dG\left(R_B, Z_B; R_f, Z_f\right)}{R_B dR_B} \times \delta I \times f \tag{5.5}$$

where the subscripts B and f denote the Mirnov coil and filament respectively, and f is the mode frequency. See Equation (2.7) for the Green's function. The locations of the filaments (black dots) and the Mirnov coils (blue squares) overlaid on the equilibrium poloidal flux contour and the $q = 2$ surface (red line) of shot #18452, at 0.306 s are shown in Figure 5.7. The magnetic island is then visualized by plotting the perturbed flux $\tilde{\psi}$ induced by the perturbed current δI superimposed on the helical flux $\psi_h = \psi_0 - \phi_0/q$ where ψ_0 and ϕ_0 are the equilibrium poloidal and toroidal flux reconstructed using VFIT.

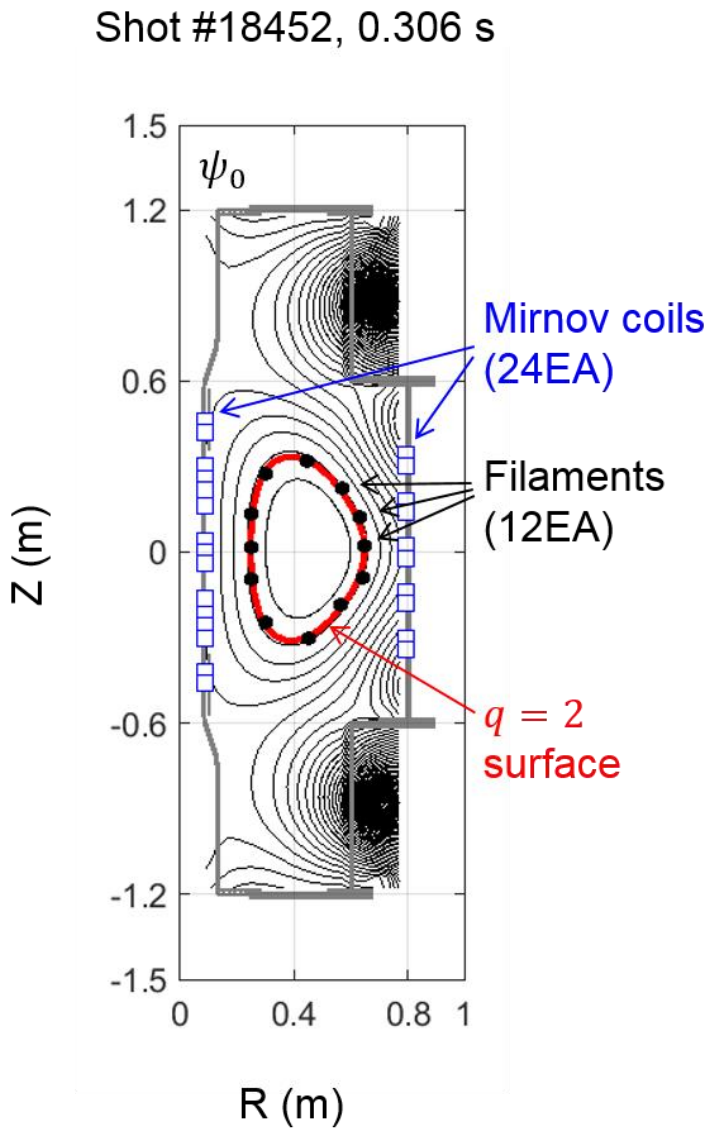

Figure 5.7 Locations of the filaments (black dots) and the Mirnov coils (blue squares) overlaid on the equilibrium poloidal flux contour and the $q = 2$ surface (red line) of shot #18452, at 0.306 s.

Filament modelling of the magnetic islands of shot #18452, at 0.306 s is shown in Figure 5.8. The locations of the Mirnov coils used for the fitting is marked with white squares, and the 4/2 (parula blue) and 3/1 (parula red) magnetic islands are overlaid on the equilibrium poloidal flux surfaces. The combination of 4/2 + 3/1 instead of 2/1 + 3/2 magnetic islands is modelled to avoid the 3/2 surface which is inaccurate when reconstructed using VFIT (see Figure 3.4). The fitted width and current of the magnetic islands are summarized in Table 5.1. The total perturbed current fraction $\left|\delta I/I_p\right|$ is 3% (plasma current is 80 kA), comparable to the normalized magnetic fluctuation as shown in Figure 4.7, and the magnetic island width is comparable to the measurements using the internal magnetic probe (Figure 3.6) and Mirnov coils (Figure 5.2).

Poloidal distribution of Mirnov coil signals of shot #18452, at 0.306 s is shown in Figure 5.9. The abscissa is the geometrical poloidal angle θ in radians. The signals from the measurements (white squares) and the reconstruction using the filament modelling (black squares) are in good agreement, except for near $\left|\theta\right| \sim 0.8$, where either the toroidal effect [64] not included in Equation (5.4) becomes significant or the filament modelling of the magnetic islands causes a singularity. The raw data of two points marked with arrows are shown in Figure 5.10. In summary, the observation of the fluctuation asymmetry along with the specific mode number combination of the coexisting magnetic islands in VEST support the existence of two magnetic islands by the neoclassical tearing mode excitation.

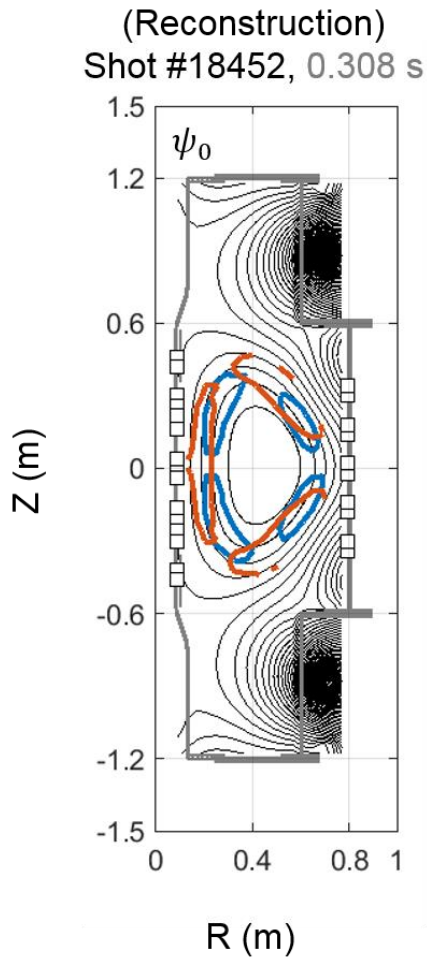

Figure 5.8 Filament modelling of the magnetic islands of shot #18452, at 0.306 s. The locations of the Mirnov coils used for the fitting is marked with white squares, and the 4/2 (parula blue) and 3/1 (parula red) magnetic islands are overlaid on the equilibrium poloidal flux surfaces. See Table 5.1 for the fit details.

Table 5.1 Filament model fitted width and current of the magnetic islands of shot #18452, at 0.306 s. The total perturbed current fraction $\left|\delta I / I_p\right|$ is 3% (plasma current is 80 kA), comparable to the normalized magnetic fluctuation as shown in Figure 4.7, and the magnetic island width is comparable to the internal magnetic probe measurements as shown in Figure 3.6. See Figure 5.8 for the contour plot.

Modes	I_0 (kA)	w (cm)
4/2	0.55	11
3/1	1.66	12

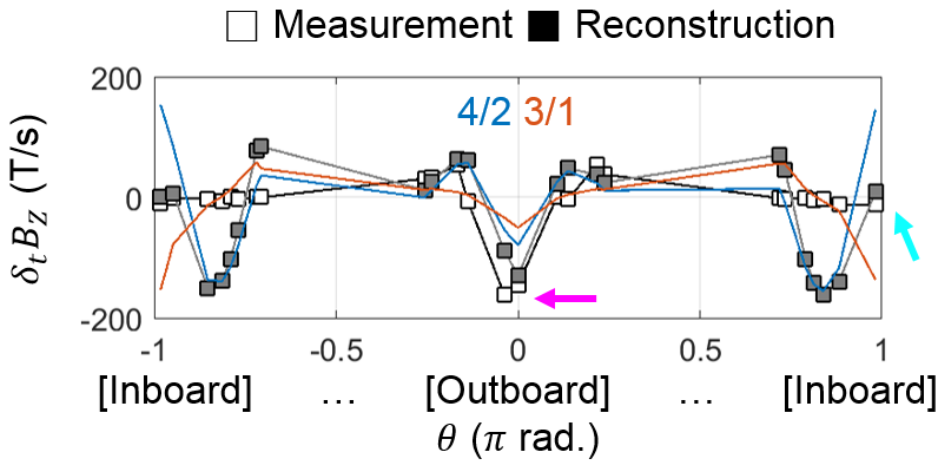

Figure 5.9 Poloidal distribution of Mirnov coil signals of shot #18452, at 0.306 s, from the measurements (white squares) and the reconstruction using the filament modelling (black squares). The abscissa is the geometrical poloidal angle θ in radians. The reconstructed signals of 4/2 (parula blue line) and 3/1 (parula red line) modes are overlaid. The raw data of two points marked with arrows are shown in Figure 5.10.

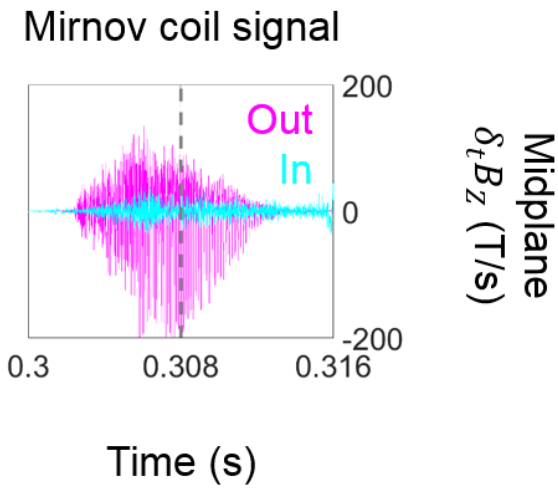

Figure 5.10 Raw data of two points marked with magenta and cyan arrows in Figure 5.9.

5.3. Stability diagram for tokamak current ramp up

Operation points at the maximum plasma current (squares) for the database of 71 shots from March to April 2018 with the maximum plasma currents over 70 kA are plotted on the $l_i - q_a$ empirical stability diagram (grey lines) [8] as shown in Figure 5.11. The internal inductance is

$$l_i = \frac{2\mu_0 W_M}{B_{pa}^2} \tag{5.6}$$

where the volume averaged magnetic energy $W_M = \int B_\theta^2 dV \Big/ 2\mu_0 \Omega$ (where $\Omega = \int dV$ is the plasma volume) and the flux surface averaged boundary field $B_{pa} = \oint B_\theta dl \Big/ \oint dl$, which are all reconstructed using VFIT. The shots with the normalized magnetic fluctuation over (i.e. tearing mode unstable) and under (i.e. tearing mode unstable) an empirical threshold of 1% are colored in red and black respectively. The $l_i - q_a$ empirical stability diagram assumes that the instability during a tokamak plasma current ramp up is the classical tearing mode, and apparently fails to explain some stable shots (e.g. shot #19160) located outside the stable region.

Comparison of the shots marked with filled squares in Figure 5.11 is shown in Figure 5.12 as the outboard midplane Mirnov coil signals, normalized beta reconstructed using VFIT, and plasma current. Note that the shots #18731 and #19157 (similar to shot #19160) are also shown in Figure 4.5 (the prefill gas pressure control experiment). Also note the apparent difference in the normalized beta. Assuming the instability during a tokamak plasma current ramp up is the neoclassical tearing mode, the stable operation space in the $l_i - q_a$ empirical stability diagram is expected to change: Based on the experimental results, the region becomes wider at

lower β_N to include e.g. shot #19160, and narrower at higher β_N to exclude e.g. shot #18731.

Plasma current ramp up in a tokamak is in general accompanied by the increase of the plasma minor radius to avoid a hollow current density profile that leads to the tearing mode onset, i.e. maintain a higher internal inductance [65]. The drawbacks of the higher internal inductance startup are: More volt second consumption (i.e. shorter pulse length) [66], less stability to vertical displacement events (i.e. smaller elongation) [67], and delayed shaping and diverting (i.e. more heat flux at the limiters) [68]. If the tearing mode can be avoided at the lower internal inductance plasma, a tokamak may be startup more efficiently, at higher elongation, and with an early shaping. The stable shots (e.g. shot #19160) located outside the stable region in the $l_i - q_a$ empirical stability diagram as shown in Figure 5.11 and the lack of magnetic island width growth at a low normalized beta plasma as shown in Figure 5.12 imply that the lower internal inductance startup is available if the normalized beta is kept low enough to avoid the neoclassical tearing mode excitation.

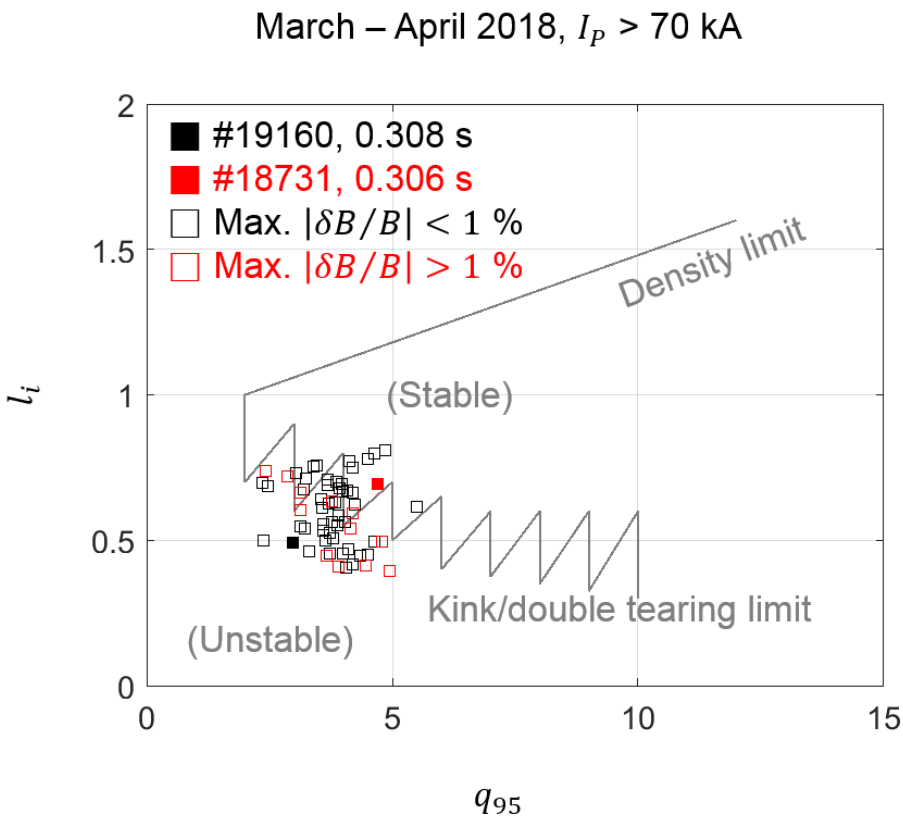

Figure 5.11 Operation points at the maximum plasma current (squares) for the database of 71 shots from March to April 2018 with the maximum plasma currents over 70 kA are plotted on the $l_i - q_a$ empirical stability diagram (grey lines) [8]. The shots with the normalized magnetic fluctuation over (i.e. tearing mode unstable) and under (i.e. tearing mode unstable) an empirical threshold of 1% are colored in red and black respectively. For the comparison of the shots marked with the filled squares, see Figure 5.12.

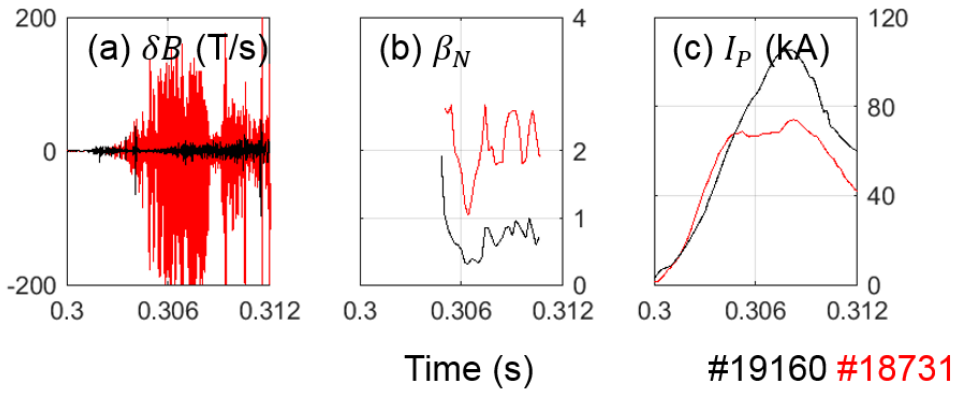

Figure 5.12 Comparison of the shots marked with filled squares in Figure 5.11. (a) Outboard midplane Mirnov coil signals. (b) Normalized beta reconstructed using VFIT. (c) Plasma current. Note that the shots #18731 and #19157 (similar to shot #19160) are also shown in Figure 4.5 (the prefill gas pressure control experiment). Also note the apparent difference in the normalized beta.

Chapter 6. Conclusion

In summary, the instability during a tokamak plasma current ramp up is introduced in Chapter 1, with Chapter 2 presenting the methods of research. Chapter 3 proves that the instability is a tearing mode. Chapter 4 shows that the classical tearing mode theory does not explain the tearing mode response to tokamak operation variables, and Chapter 5 argues the neoclassical features of the tearing modes, from which a startup scheme is suggested.

In conclusion, this dissertation presents the first direct measurement of the instability during a tokamak plasma current ramp up. A comprehensive picture is provided using both the internal and external magnetic diagnostics, which is made available primarily by the development of the equilibrium reconstruction technique for the early phase of a tokamak operation compatible with the internal magnetic probes. This dissertation also presents that the instability is a tearing mode with the neoclassical features: The magnetic island width is modelled with the modified Rutherford equation including the bootstrap current drive term, and the fluctuation asymmetry from the phase alignment of the nonlinear toroidal coupled magnetic islands is observed. This dissertation finally presents that the neoclassical aspects of the instability should be considered in the development of the tokamak plasma current ramp up scenario.

Bibliography

[1] H. Bethe, "Energy production in stars," *Physical Review,* vol. 55, p. 434, 1939.

[2] L. Artsimovich, "Tokamak devices," *Nuclear Fusion,* vol. 12, p. 215, 1972.

[3] N. Peacock, D. Robinson, M. Forrest, P. Wilcock and V. Sannikov, "Measurement of the electron temperature by Thomson scattering in tokamak T3," *Nature,* vol. 224, p. 488, 1969.

[4] J. Menard, B. LeBlanc, S. Sabbagh, M. Bell, R. Bell, E. Fredrickson, D. Gates, S. Jardin, D. Johnson, S. Kaye, H. Kugel, R. Maingi, R. Maqueda, D. Mueller, M. Ono, F. Paoletti, S. Paul, C. Skinner and D. Stutman, "Ohmic flux consumption during initial operation of the NSTX spherical torus," *Nuclear Fusion,* vol. 41, p. 1197, 2001.

[5] H. Furth, J. Killeen and M. Rosenbluth, "Finite-resistivity instabilities of a sheet pinch," *Physics of Fluids,* vol. 6, p. 459, 1963.

[6] R. Bickerton, J. Connor and J. Taylor, "Diffusion driven plasma currents and bootstrap tokamak," *Nature Physical Science,* vol. 229, p. 110, 1971.

[7] Z. Chang, J. Callen, E. Fredrickson, R. Budny, C. Hegna, K. McGuire and M. Zarnstorff, "Observation of nonlinear neoclassical pressure-gradient-driven tearing modes in TFTR," *Physical Review Letters,* vol. 74, p. 4663, 1995.

[8] J. Wesson, R. Gill, M. Hugon, F. Schuller, J. Snipes, D. Ward, D. Bartlett, D. Campbell, P. Duperrex, A. Edwards, R. Granetz, N. Gottardi, T. Hender, E. Lazzaro, P. Lomas, N. Lopes Cardozo, K. Mast, M. Nave, N. Salmon, P.

Smeulders, P. Thomas, B. Tubbing, M. Turner and A. Weller, "Disruptions in JET," *Nuclear Fusion,* vol. 29, p. 641, 1989.

[9] K. Toi, S. Itoh, K. Kadota, K. Kawahata, N. Noda, K. Sakurai, K. Sato, S. Tanahashi and S. Yasue, "Current density profile control by programming of gas puffing and plasma current waveform in the JIPP T-II tokamak," *Nuclear Fusion,* vol. 19, p. 1643, 1979.

[10] A. Scarabosio, A. Pochelon and Y. Martin, "Plasma shape stabilization of current rise MHD instabilities in TCV," *Plasma Physics and Controlled Fusion,* vol. 49, p. 1041, 2007.

[11] R. La Haye, R. Buttery, S. Guenter, G. Huysmans, M. Maraschеck and H. Wilson, "Dimensionless scaling of the critical beta for onset of a neoclassical tearing mode," *Physics of Plasmas,* vol. 7, p. 3349, 2000.

[12] A. Costley, R. Hastie, J. Paul and J. Chamberlain, "Electron cyclotron emission from a tokamak plasma: experiment and theory," *Physical Review Letters,* vol. 33, p. 758, 1974.

[13] J. Slough and K. Miller, "Small, high frequency probe for internal magnetic field measurements in high temperature plasmas," *Review of Scientific Instruments,* vol. 72, p. 417, 2001.

[14] J. Yang, J. Lee, B. Jung, K. Chung and Y. Hwang, "Development of internal magnetic probe for current density profile measurement in Versatile Experiment Spherical Torus," *Review of Scientific Instruments,* vol. 85, p. 11D809, 2014.

[15] I. Hutchinson, "Magnetic probe investigation of the disruptive instability in tokamak LT-3," *Physical Review Letters,* vol. 37, p. 338, 1976.

[16] L. Giannone, R. Cross and I. Hutchinson, "Internal magnetic probe measurements of MHD activity and current profiles in a tokamak," *Nuclear Fusion,* vol. 27, p. 2085, 1987.

[17] D. Robinson and K. McGuire, "Magnetic islands and disruptions in the TOSCA tokamak," *Nuclear Fusion,* vol. 19, p. 115, 1979.

[18] H. Zhong, Y. Tan and Z. Gao, "Experimental study of the tearing mode instability during the current ramp up stage in Sino-United Spherical Tokamak," *Nuclear Fusion,* vol. 58, p. 126013, 2018.

[19] K. Chung, Y. An, B. Jung, H. Lee, C. Sung, Y. Na, T. Hahm and Y. Hwang, "Design features and commissioning of the Versatile Experiment Spherical Torus (VEST) at Seoul National University," *Plasma Science and Technology,* vol. 15, p. 244, 2013.

[20] Y. An, J. Lee, J. Jo, B. Jung, H. Lee, K. Chung, Y. Na, T. Hahm and Y. Hwang, "Efficient ECH-assisted plasma start-up using trapped particle configuration in the Versatile Experiment Spherical Torus," *Nuclear Fusion,* vol. 57, p. 016001, 2017.

[21] L. Lao, H. John, R. Stambaugh, A. Kellman and W. Pfeiffer, "Reconstruction of current profile parameters and plasma shapes in tokamaks," *Nuclear Fusion,* vol. 25, p. 1611, 1985.

[22] D. Swain and G. Neilson, "An efficient technique for magnetic analysis of non-circular, high-beta tokamak equilibria," *Nuclear Fusion,* vol. 22, p. 1015, 1982.

[23] F. Hofmann and G. Tonetti, "Fast identification of plasma boundary and x-points in elongated tokamaks," *Nuclear Fusion,* vol. 28, p. 519, 1988.

[24] J.-M. Moret, B. Duval, H. Le, S. Coda, F. Felici and H. Reimerdes, "Tokamak equilibrium reconstruction code LIUQE and its real time implementation," *Fusion Engineering and Design,* vol. 91, p. 1, 2015.

[25] Y. An, J. Lee, H. Lee, J. Jo, B. Jung, K. Chung, Y. Kim, J. Jo, J. Yang, Y. Na, T. Hahm and Y. Hwang, "Plasma start-up design and first plasma experiment in VEST," *Fusion Engineering and Design,* vol. 96, p. 274, 2015.

[26] S. Sabbagh, S. Kaye, J. Menard, F. Paoletti, M. Bell, R. Bell, J. Bialek, M. Bitter, E. Fredrickson, D. Gates, A. Glasser, H. Kugel, L. Lao, B. LeBlanc, R. Maingi, R. Maqueda, E. Mazzucato, D. Mueller, M. Ono, S. Paul, M. Peng, C. Skinner, D. Stutman, G. Wurden and W. Zhu, "Equilibrium properties of spherical torus plasmas in NSTX," *Nuclear Fusion,* vol. 41, p. 1601, 2001.

[27] T. Ushiki, M. Inomoto and M. Itagaki, "Reconstruction of plasma shape and eddy current profile based on modified Cauchy condition surface method in merging spherical tokamak," *Fusion Engineering and Design,* vol. 122, p. 35, 2017.

[28] Y. Jeon, "Development of a free-boundary tokamak equilibrium solver for advanced study of tokamak equilibria," *Journal of the Korean Physical Society,* vol. 67, p. 843, 2015.

[29] M. Hole and L. Appel, "Fourier decomposition of magnetic perturbations in toroidal plasmas using singular value decomposition," *Plasma Physics and Controlled Fusion,* vol. 49, p. 1971, 2007.

[30] C. Nardone, "Multichannel fluctuation data analysis by the singular value decomposition method and application to MHD modes in JET," *Plasma Physics and Controlled Fusion,* vol. 34, p. 1447, 1992.

[31] J. Kim, D. Edgell, J. Greene, E. Strait and M. Chance, "MHD mode identification of tokamak plasmas from Mirnov signals," *Plasma Physics and Controlled Fusion,* vol. 41, p. 1399, 1999.

[32] I. Duran, J. Stockel, G. Mank, K. Finken, G. Fuchs and G. Van Oost, "Measurements of magnetic field fluctuations using an array of Hall detectors on the TEXTOR tokamak," *Review of Scientific Instruments,* vol. 73, p. 3482, 2002.

[33] C. Romero-Talamas, P. Bellan and S. Hsu, "Multielement magnetic probe using commercial chip inductors," *Review of Scientific Instruments,* vol. 75, p. 2664, 2004.

[34] Y. Liu, D. Maurer, G. Navratil and N. Rivera, "High spatial resolution Hall sensor array for edge plasma magnetic field measurements," *Review of Scientific Instruments,* vol. 76, p. 093501, 2005.

[35] M. Bongard, R. Fonck, B. Lewicki and A. Redd, "A Hall sensor array for internal current profile constraint," *Review of Scientific Instruments,* vol. 81, p. 10E105, 2010.

[36] J. Yang, K. Chung, Y. An, B. Jung, J. Jo and Y. Hwang, "Design of a dual sensor probe array for internal field measurement in Versatile Experiment Spherical Torus," *Review of Scientific Instruments,* vol. 83, p. 10D721, 2012.

[37] M. Schittenhelm and H. Zohm, "Analysis of coupled MHD modes with Mirnov probes in ASDEX Upgrade," *Nuclear Fusion,* vol. 37, p. 1255, 1997.

[38] T. Stix, "Current penetration and plasma disruption," *Physical Review Letters,* vol. 36, p. 521, 1976.

[39] Q. Yu, Y. Gunter, K. Lackner, A. Gude and M. Maraschеck, "Interactions between neoclassical tearing modes," *Nuclear Fusion,* vol. 40, p. 2031, 2000.

[40] P. Rutherford, "Nonlinear growth of the tearing mode," *Physics of Fluids,* vol. 16, p. 1903, 1973.

[41] O. Sauter, R. La Haye, Z. Chang, D. Gates, Y. Kamada, H. Zohm, A. Bondeson, D. Boucher, J. Callen, M. Chu, T. Gianakon, O. Gruber, R. Harvey, C. Hegna, L. Lao, D. Monticello, F. Perkins, A. Pletzer, A. Reiman, M. Rosenbluth, E. Strait, T. Taylor, A. Turnbull, F. Waelbroeck, J. Wesley, H. Wilson and R. Yoshino, "Beta limits in long-pulse tokamak discharges," *Physics of Plasmas,* vol. 4, p. 1654, 1997.

[42] Y. Tan, G. Yang, H. Xie, Y. Liu, R. Ke, Y. Jiang, S. Chai, W. Wang and Z. Gao, "An ohmic field power supply based on a modified IGBT H-bridge for Sinu-UNited Spherical Tokamak," *Fusion Engineering and Design,* vol. 98, p. 1163, 2015.

[43] B. Heim, S. Gonderman, C. Taylor, J. Allain, Z. Yang, M. Gonzalez, E. Collins, C. Skinner, B. Ellis, W. Blanchard, L. Roquemore, H. Kugel, R. Martin and R. Kaita, "The Materials Analysis Particle Probe (MAPP) diagnostic system in NSTX," *IEEE Transactions on Plasma Science,* vol. 40, p. 735, 2012.

[44] R. Colchin, D. Hillis, R. Maingi, C. Klepper and N. Brooks, "The filterscope," *Review of Scientific Instruments,* vol. 74, p. 2068, 2003.

[45] C. Skinner, F. Bedoya, F. Scotti, J. Allain, W. Blanchard, D. Cai, M. Jaworski and B. Koel, "Advances in boronization on NSTX-Upgrade," *Nuclear Materials and Energy,* vol. 12, p. 744, 2017.

[46] W. Suttrop, K. Buchi, J. Fuchs, M. Kaufmann, K. Lackner, M. Maraschеck, V. Mertens, R. Neu, M. Schittenhelm, M. Sokoll and H. Zohm, "Tearing mode formation and radiative edge cooling prior to density limit disruptions in ASDEX Upgrade," *Nuclear Fusion,* vol. 37, p. 119, 1997.

[47] P. Rebut and M. Hugon, "Thermal instability and disruptions in a tokamak," *Plasma Physics and Controlled Nuclear Fusion Research,* vol. 2, p. 197, 1985.

[48] Y.-K. Peng and D. Strickler, "Features of spherical torus plasmas," *Nuclear Fusion,* vol. 26, p. 769, 1986.

[49] M. Gryaznevich, R. Akers, P. Carolan, N. Conway, D. Gates, A. Field, T. Hender, I. Jenkins, R. Martin, M. Nightingale, C. Ribeiro, D. Robinson, A. Sykes, M. Tournianski, M. Valovic and M. Walsh, "Achievement of record beta in the START spherical tokamak," *Physical Review Letters,* vol. 80, p. 3972, 1998.

[50] A. Glasser, J. Greene and J. Johnson, "Resistive instabilities in a tokamak," *Physics of Fluids,* vol. 19, p. 567, 1976.

[51] R. La Haye, R. Buttery, S. Gerhardt, S. Sabbagh and D. Brennan, "Aspect ratio effects on neoclassical tearing modes from comparison between DIII-D and National Spherical Torus Experiment," *Physics of Plasmas,* vol. 19, p. 062506, 2012.

[52] A. Pletzer, A. Bondeson and R. Dewar, "Linear stability of resistive MHD modes: Axisymmetric toroidal computation of the outer region matching data," *Journal of Computational Physics,* vol. 115, p. 530, 1994.

[53] H. Lutjens, A. Bondeson and O. Sauter, "The CHEASE code for toroidal MHD equilibria," *Computer Physics Communications,* vol. 97, p. 219, 1996.

[54] R. La Haye, "Neoclassical tearing modes and their control," *Physics of Plasmas,* vol. 13, p. 055501, 2006.

[55] H. Reimerdes, O. Sauter, T. Goodman and A. Pochelon, "From current-driven to neoclassically driven tearing modes," *Physical Review Letters,* vol. 88, p. 105005, 2002.

[56] G. Garstka, S. Diem, R. Fonck, B. Lewicki, A. Sontag, K. Tritz and E. Unterberg, "Performance and stability of near-unity aspect ratio plasmas in the Pegasus Toroidal Experiment," *Physics of Plasmas,* vol. 10, p. 1705, 2003.

[57] R. Fitzpatrick, "Phase locking of multi-helicity neoclassical tearing modes in tokamak plasmas," *Physics of Plasmas,* vol. 22, p. 042514, 2015.

[58] B. Tobias, M. Chen, I. Classen, C. Domier, R. Fitzpatrick, B. Grierson, N. Luhmann, C. Muscatello, M. Okabayashi, K. Olofsson and C. Paz-Soldan, "Rotation profile flattening and toroidal flow shear reversal due to the coupling of magnetic islands in tokamaks," *Physics of Plasmas,* vol. 23, p. 056107, 2016.

[59] G. Kim, G. Yun, M. Woo and H. Park, "Interactions of toroidally coupled tearing modes in the KSTAR tokamak," *Plasma Physics and Controlled Fusion,* vol. 60, p. 035009, 2018.

[60] T. Harley, D. Buchenauer, J. Coonrod and K. McGuire, "TFTR Mirnov coil analysis with toroidal effects at plasma startup," *Nuclear Fusion,* vol. 29, p. 771, 1989.

[61] O. Kluber, H. Zohm, H. Bruhns, J. Gernhard, A. Kallenbach and H. Zehrfeld, "MHD mode structure and propagation in the ASDEX tokamak," *Nuclear Fusion,* vol. 31, p. 907, 1991.

[62] C. Chen, S. Sun, X. Ji and Z. Yin, "Development of a real time magnetic island identification system for HL-2A tokamak," *Review of Scientific Instruments,* vol. 88, p. 083510, 2017.

[63] H. Zohm, G. Gantenbein, G. Giruzzi, S. Gunter, F. Leuterer, M. Maraschеck, J. Meskat, A. Peeters, W. Suttrop, D. Wagner and M. Zabiego, "Experiments on neoclassical tearing mode stabilization by ECCD in ASDEX Upgrade," *Nuclear Fusion,* vol. 39, p. 577, 1999.

[64] V. Merezhkin, "Structure of the magnetic-field perturbations in the disruptive instability in the T-6 tokamak," *Soviet Journal of Plasma Physics,* vol. 4, p. 152, 1978.

[65] D. Mueller, "The physics of tokamak start-up," *Physics of Plasmas,* vol. 20, p. 058101, 2013.

[66] S. Ejima, R. Callis, J. Luxon, R. Stambaugh, T. Taylor and J. Wesley, "Volt-second analysis and consumption in Doublet III plasmas," *Nuclear Fusion,* vol. 22, p. 1313, 1982.

[67] J. Menard, M. Bell, R. Bell, D. Gates, S. Kaye, B. LeBlanc, R. Maingi, S. Sabbagh, V. Soukhanovskii and D. Stutman, "Aspect ratio scaling of ideal no-wall stability limits in high bootstrap fraction tokamak plasmas," *Physics of Plasmas,* vol. 11, p. 639, 2004.

[68] G. Jackson, T. Casper, T. Luce, D. Humphreys, J. Ferron, A. Hyatt, E. Lazarus, R. Moyer, T. Petrie, D. Rudakov and W. West, "ITER startup studies in the DIII-D tokamak," *Nuclear Fusion,* vol. 48, p. 125002, 2008.

Abstract in Korean

토카막 플라즈마 전류 상승기의 찢어짐 모드

토카막은 플라즈마를 자기장과 플라즈마 전류로 가두어 핵융합 에너지를 추출하는 개념이다. 빠른 플라즈마 전류 상승은 빠른 시변 구동 일주 전압으로부터의 표피 효과에 의해 형성된 속이 빈 전류 밀도 프로파일이 만드는 찢어짐 모드로 예상되는 자기유체역학적 플라즈마 불안정성에 의해 방해된다고 알려져 있다. 이 예상을 확인하기 위해서는 차갑고 변화하는 플라즈마 전류 상승기의 불안정성에 대한 종합적 진단이 필요하다. 내부 자기장 프로브가 차가워서 섭동이 저은 플라즈마의 자기섬의 직접 진단하기 위해 사용된다. 기존에는 내부 자기장 프로브를 사용할 수 있는 작은 장치에서 평형 자기면 정보가 안정적으로 얻어지지 않았기 때문에 측정의 해석에 어려움이 있었다. VEST 에서의 플라즈마 전류 상승기에, 미르노프 코일의 분광도에는 특이한 불안정성 패턴이 나타난다. 이 논문에서는 토카막 플라즈마 전류 상승기의 불안정성을 연구한다.

VEST 는 주반경 0.4 m, 부반경 0.3 m, 자기축 토로이달 자기장 0.1 T, 그리고 플라즈마 전류 0.1 MA 를 나타내는 구형 토러스이다. TF 코일은 울트라캐패시터 뱅크로, PF 코일은 선결 시간에 스위칭되는 축전기 뱅크로 구동된다. PEV 가 일주 전압 인가 전에 선입 가스를 주입한다. VEST 의 자기 진단은 플라즈마 내부와 외부에 있다. 11 개의 자속 루프와 49 개의 자기 프로브가 폴로이달 평면에 분포되어 있다.

자속 루프는 25 kS/s, 자기 프로브는 250 kS/s 로 디지털화한다. 평형 자속면은 다양한 진단을 하나의 틀로 연결한다. 평형 재구성 코드 VFIT 이 그라드 샤프라노프 방정식의 자유 경계 해를 찾는 알고리즘을 구현하기 위해 개발되었다. 실제 데이터에는 신호와 잡음이 섞여 있어 세심한 구분이 필요하다. 12 개의 사각형 요소가 플라즈마 전류 분포를 모사하기 위해 사용되었고 각 요소의 전류가 코일 전류와 같이 플라즈마에 의한 벽 전류를 계산하는 데 사용되었다. VFIT 실행 결과, 측정기 신호가 평균 10% 까지 맞추어졌고 수렴 조건은 10^{-3} 으로 설정되었다. 유용한 평형 파라미터가 재구성된 평형 자속면으로부터 후처리될 수 있다. 자기적 진동의 모드 정보는 불안정성의 특징을 내포한다. 2 개의 미르노프 코일로 된 토로이달 배열은 푸리에 분석되어 토로이달 모드수와 주파수 정보를 준다. 25 개의 미르노프 코일로 된 폴로이달 배열은 특이값 분해되어 폴로이달 모드수를 준다. 모드 분석은 0.2 ms 마다 1 ms 창으로 시행된다. VEST 에서는 내부 자기장 프로브에 의한 플라즈마 전류 하강이 10%를 넘지 않는데, 플라즈마 크기와 에너지가 작기 때문으로 보인다. 측정기 그룹은 홀 센서 하나와 칩 인덕터 두 개로 구성되고, 총 8 개의 그룹이 중앙면에서 0.30 m 이상의 반경을 0.05 m 간격으로 측정한다. 측정기 지지는 인쇄 회로 기판이 사용되었다. 내부 자기장 프로브의 겉면은 스테인리스 스틸 파이프와 알루미나 튜브가 정전기적 그리고 열적 차폐를 제공하도록 구성된다. 내부 자기장 프로브의 교정은 세 단계로 이루어진다: 헬름홀츠 코일, 어긋남 각도, 반경 위치가 그것들이다.

토카막에서 자기섬은 특징적인 시변 자기장 구조를 만든다. 내부 자기장 프로브 측정은 위상 역전 구조를 보여주어 자기섬의 존재를

뒷받침한다. 내부 및 외부 프로브로 측정된 위상 역전과 섬열 위치는 서로 잘 일치한다. 그러면 자기섬의 역학이 내부 자기장 프로브로 연구될 수 있다. 두 개의 자기섬은 동시에 발생하여 서로에게 위상이 맞추어지고 주 플라즈마와 모두 함께 내벽으로 이동한다. 자기섬들이 위상이 맞추어진 채 함께 움직인다는 것은 흥미로운데, 기존 이해는 인접한 자기섬들이 합쳐지는 것이기 때문이다. 자기섬 폭은 일반적으로 외부 미르노프 코일 신호에 직접 측정을 통해 교정되어 연결된다. 그러면 내부 자기장 프로브가 없더라도 외부 미르노프 코일 신호 의해 섬폭이 근사될 수 있다.

고전 찢어짐 모드 이론으로 전류 상승 속도 제어에 대한 찢어짐 모드 반응이 설명된다. 이 때, 선주입 기체 압력과 벽 조건이 적절히 통제되었다. 고전 찢어짐 모드 이론을 이용한 해석을 더욱 밝히기 위해, 국지적인 자기 전단 자체를 제어하는 실험이 설계되었다. 고전 찢어짐 모드 이론의 예측대로, 어떤 모드의 발생과 소멸은 해당 자기 플럭스면의 자기 전단의 변화와 일치한다. 고전 찢어짐 모드 이론이 찢어짐 모드의 전류 상승 속도 제어에 대한 반응을 잘 설명하지만, 찢어짐 모드의 선주입 기체 압력 제어에 대한 반응을 설명하는 데는 실패한다. 이 때, 전류 상승 속도와 플라즈마 모양이 적절히 통제되었다. 피어슨 상관 계수를 비교하면, 선주입 기체 압력은 전류 상승 속도만큼이나 찢어짐 모드 제어에 대해서 효과적인 제어 손잡이이다. VEST 에서는 신고전 찢어짐 모드 이론이 전류 상승 속도와 선주입 기체 압력에 의한 플라즈마 전류 상승기의 찢어짐 모드 제어를 설명할 것으로 예상된다.

자기섬의 성장은 일반적으로 수정 러더포드 방정식으로 모사된다. VFIT 과 PEST-3 가 수정 러더포드 방정식의 변수들을 계산하기 위해 사용되었다. 2/1 모드 자기섬이 추적되었는데, 작은 자기섬 효과 요소는 6 cm 로 고정하였다. 2/1 모드 자기섬 성장을 모사한 것과 측정한 것은 서로 잘 일치하여 신고전 찢어짐 모드의 존재를 뒷받침한다. VEST 자기섬들은 특정 모드 수 조합을 갖는데, 처음에는 2/1 + 3/2 이고 그 후에는 3/1 + 4/2 이며, 역시 신고전 찢어짐 모드의 존재를 뒷받침한다. 불안정성 비대칭성을 관찰한다면 두 자기섬이 신고전 찢어짐 모드에 의해 발생해 공존함을 뒷받침할 것이다. 내부 자기장 프로브와 외부 미르노프 코일에 의해 불안정성 비대칭성이 관찰되었다. 기존에는 내부 측정이 없었기 때문에 관찰의 진위가 불확실했다. 자기섬의 필라멘트 모델을 통해 불안정성 비대칭성을 모사하였다. 4/2 + 3/1 모드 조합이 2/1 + 3/2 모드 조합 대신 합리적으로 모사되었다. 측정 및 필라멘트 모델로 재구성된 미르노프 코일 신호의 폴로이달 분포가 잘 일치하여, 두 자기섬이 신고전 찢어짐 모드에 의해 발생해 공존함을 뒷받침한다. 정규화 내부 유도용량과 가장자리 안전 인자로 표현된 경험적 안정성 도표는 토카막 플라즈마 전류 상승기의 불안정성이 고전 찢어짐 모드라고 가정하지만, 일부 안정 영역 밖의 샷들을 설명하는 데 실패한다. 실험 결과를 바탕으로 살펴보면 안전 영역이 낮은 정규화 베타일 때 넓어지고 높은 정규화 베타일 때 좁아진다. 그러면, 정규화 베타가 낮게 유지되어 신고전 찢어짐 모드의 발생을 피한다면 더 낮은 정규화 내부 유도용량 시동이 가능하다.

주요어: 토카막 시동.
VEST.
내부 자기장 프로브.
평형 재구성.
자기섬.
찢어짐 모드.
수정 러더포드 방정식.
섭동 비대칭성.
신고전 찢어짐 모드.
$l_i - q_a$ 안정성 도표.

학번: 2013-30996